

A fast algorithm for the wave equation using time-windowed Fourier projection

Nour G. Al Hassanieh^{a,b}, Alex H. Barnett^a, Leslie Greengard^{a,b}

^aCenter for Computational Mathematics, Flatiron Institute, Simons Foundation, New York, New York 10010

^bCourant Institute of Mathematical Sciences, New York University, New York, New York 10012

Abstract

We introduce a new arbitrarily high-order method for the rapid evaluation of hyperbolic potentials (space-time integrals involving the Green's function for the scalar wave equation). With M points in the spatial discretization and N_t time steps of size Δt , a naive implementation would require $\mathcal{O}(M^2 N_t^2)$ work in dimensions where the weak Huygens' principle applies. We avoid this all-to-all interaction using a smoothly windowed decomposition into a local part, treated directly, plus a history part, approximated by a N_F -term Fourier series. In one dimension, our method requires $\mathcal{O}((M + N_F \log N_F) N_t)$ work, with $N_F = \mathcal{O}(1/\Delta t)$, by exploiting the non-uniform fast Fourier transform. We demonstrate the method's performance for time-domain scattering problems involving a large number M of springs (point scatterers) attached to a vibrating string at arbitrary locations, with either periodic or free-space boundary conditions. We typically achieve 10-digit accuracy, and include tests for M up to a million.

Keywords: wave equation, hyperbolic potential theory, Volterra integral equation, window function, point scatterer, high order

1. Introduction

In this paper, we consider the scalar wave equation in one space dimension, posed either in free space ($x \in \mathbb{R}$) or in a periodic box ($x \in B$, with $B = [-\pi, \pi]$). This equation governs the propagation of waves on a string, where the function of interest is the displacement of the string in the vertical direction. It also governs linear acoustics and (through a slight generalization) time-dependent electromagnetics. The numerical solution of such wave problems, especially the two- and three-dimensional (3D) cases, and especially at high frequency (many wavelengths across the domain), are extremely useful in engineering applications. We are particularly interested in advancing the integral equation approach [1]. The acceleration techniques we present do generalize to higher dimensions, but the application to scattering demands other complications such as spatial quadratures. Thus we chose to present the ideas in the setting of a high-order accurate solution of a 1D model problem, but one which retains the challenges of high frequencies and multiple scattering.

While the pure initial value problem for the wave equation admits an analytic solution [2, Ch. 4 & 10], most problems of interest involve boundary and/or interface conditions. We consider point-like scatterers for 1D waves. At each point x_j in a collection $\Gamma = \{x_j\}_{j=1}^M \subset B$, the string is attached vertically to a fixed reference by a spring of nondimensionalized spring constant $\beta_j > 0$, as sketched in Fig. 1. (The natural length of the spring is chosen such that its force is zero when the string is quiescent.) A given rightward-traveling solution of the homogeneous wave equation

$$u_{\text{inc}}(x, t) = f(x - t) \tag{1}$$

then impinges on this structure. We will assume that f is smooth and that $\Gamma \cap \text{supp } f = \emptyset$. In the standard scattering theory setup, the total (physical) displacement is written in the form

$$u_{\text{tot}}(x, t) = u_{\text{inc}}(x, t) + u(x, t),$$

Email addresses: nalhassanieh@flatironinstitute.org (Nour G. Al Hassanieh), abarnett@flatironinstitute.org (Alex H. Barnett), lgreengard@flatironinstitute.org (Leslie Greengard)

where $u(x, t)$ is the *scattered field*. It is straightforward to show (in the free-space setting) that $u(x, t)$ must satisfy the following boundary value problem (BVP):

$$\partial_t^2 u - \partial_x^2 u = 0, \quad x \in \mathbb{R} \setminus \Gamma, \quad t > 0, \quad (2)$$

$$u(x, 0) = \partial_t u(x, 0) = 0, \quad x \in \mathbb{R}, \quad (3)$$

$$[u](x_j, t) = 0, \quad j = 1, \dots, M, \quad t > 0, \quad (4)$$

$$[\partial_x u](x_j, t) - \beta_j u(x_j, t) = g_j(t), \quad j = 1, \dots, M, \quad t > 0. \quad (5)$$

Here the square parenthesis

$$[s](x_j, t) \equiv \lim_{\epsilon \rightarrow 0} s(x_j + \epsilon, t) - s(x_j - \epsilon, t)$$

denotes the spatial jump in a function s at position x_j and time t . The time-dependent driving functions are

$$g_j(t) := \beta_j u_{\text{inc}}(x_j, t) - [\partial_x u_{\text{inc}}](x_j, t), \quad (6)$$

specified by the incident field. The Cauchy matching conditions at the spring locations x_j correspond to continuity, and to vertical force balance at the (massless) point x_j . Specifically, the physical string displacement satisfies

$$[\partial_x u_{\text{tot}}](x_j, t) = \beta_j u_{\text{tot}}(x_j, t),$$

where the left side comes from tension in the string while the right side is the spring restoring force. Notice that the limit $\beta_j \rightarrow +\infty$ would be a completely reflective Dirichlet condition allowing no communication between the regions $x < x_j$ and $x > x_j$. Finite β_j gives partial reflection and partial transmission, and is possibly the simplest nontrivial point scatterer in 1D.¹ Such scatterers model localized impurities in an otherwise homogeneous medium, and hence have been studied in the physics and acoustics community [3, 5–7]. Precisely the same “delta potential” scatterer model is also analyzed in quantum mechanics in one or more dimensions [8, 9].

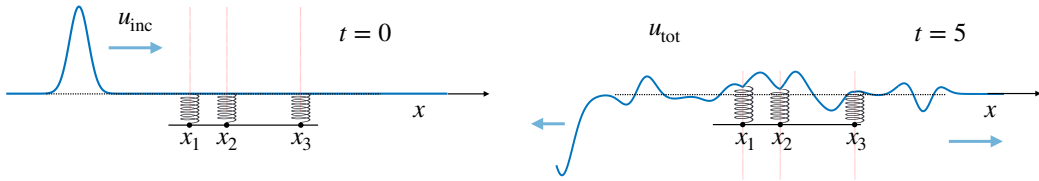


Figure 1: (Left) A wideband pulse propagates rightwards along an infinite string, and impinges on a region where the string is attached to a set of springs, i.e., point-like scatterers. (The equilibrium position aligns with the quiescent string.) (Right) The total displacement is plotted at a later time after the initial pulse has traversed the springs. Note that the displacement is continuous but not smooth. (The jump in slope is most visible at the locations of the first two springs.)

Our interest in this problem, aside from the physics itself, is that it will allow us to investigate integral equation methods based on *hyperbolic layer potentials* in a simple setting. For this, we represent $u(x, t)$ as a *single layer potential*:

$$u(x, t) = \mathcal{S}[\Gamma, \vec{\sigma}](x, t) = \sum_{j=1}^M \int_0^t G(x - x_j, t - \tau) \sigma_j(\tau) d\tau = \frac{1}{2} \sum_{j=1}^M \int_0^{t - |x - x_j|} \sigma_j(\tau) d\tau, \quad x \in \mathbb{R}, \quad t > 0, \quad (7)$$

where $\vec{\sigma}(t) = \{\sigma_1(t), \dots, \sigma_M(t)\}$, each $\sigma_j(t)$ is an unknown *density* and $G(x, t)$ is the free-space Green’s function for the 1D wave equation:

$$G(x, t) = \frac{1}{2} H(t - |x|), \quad (8)$$

¹This scatterer can also be realised as the zero-width limit of a narrow and tall potential function. A related simple point scatterer model is a “bead on a string” [3] [4, Ch. 1].

where $H(x)$ as usual denotes the Heaviside step function

$$H(x) = \begin{cases} 1, & x \geq 0 \\ 0, & x < 0. \end{cases}$$

With this representation, $u(x, t)$ satisfies (2)–(4). Imposing the derivative jump (5) using the jump relation

$$[\partial_x u](x_j, t) = -\sigma_j(t) \quad (9)$$

for the single-layer representation [2, §10.6], yields after a little algebra a system of Volterra integral equations for the unknown densities $\sigma_j(t)$:

$$-\sigma_j(t) - \frac{\beta_j}{2} \sum_{l=1}^M \int_0^{t-|x_j-x_l|} \sigma_l(\tau) d\tau = g_j(t), \quad j = 1, \dots, M, \quad t > 0. \quad (10)$$

Once the functions $\sigma_j(t)$ are known, the scattered field can be evaluated at any desired point using (7).

There are several advantages to the integral formulation of the wave equation. First, it requires a discretization of the boundary alone (here, the points x_j). Second, the order of accuracy of the scheme is determined by the order of accuracy of the quadrature in time, with no numerical dispersion error. Third, it captures the piecewise-smooth structure of the solution analytically.

An obvious disadvantage of this approach is the history-dependence of the layer potentials: at a given time $t = n\Delta t$, evaluating the representation (7) at a set of M target points—or its derivative jumps, as required in the left-hand side of (10), would require $\mathcal{O}(M^2 n)$ work in a naive implementation. Thus, the full simulation would require of the order $\mathcal{O}(M^2 N_t^2)$ work. Moreover, it would require $\mathcal{O}(MN_t)$ storage for the history of the densities at all time steps.

Remark 1.1. *In one space dimension (1D), it is easy to see that $u(x, t)$ satisfies the recurrence*

$$u(x, t + \Delta t) = u(x, t) + \sum_{j=1}^M \int_{t-|x-x_j|}^{t+\Delta t-|x-x_j|} \sigma_j(\tau) d\tau.$$

This would reduce the cost of evaluating the representation to $\mathcal{O}(M^2)$ work per timestep, for a total work of $\mathcal{O}(M^2 N_t)$, and $\mathcal{O}(M/\Delta t)$ storage. Such a simple acceleration is not available in 2D, due to the weak Huygens’ principle, while in 3D the strong Huygens’ principle would yield a similar improvement without any recurrence (as in, e.g., [10]). In all cases the cost per time step remains quadratic in M .

The main contribution of the present paper is a new time-marching method for the wave equation—windowed Fourier projection (WFP)—that is independent of spatial dimension, eliminates the history dependence, requires modest storage, and whose cost per time step scales quasi-linearly in the number of scatterers M . More precisely, we will make use of a Fourier series with $N_F = \mathcal{O}(1/\Delta t)$ modes, in the 1D case, to represent the history contribution to the representation. The remaining “local” part requires densities only $\mathcal{O}(\Delta t)$ into the past. The densities and modes evolve in a coupled integro-differential system that may be efficiently time-marched. We will show that the total amount of work for our scheme is $\mathcal{O}((M + N_F \log N_F) N_t)$, assuming that springs are more or less uniformly distributed and that $\Delta t \lesssim 1/M$ (these latter conditions ensuring that the local part has linear cost).

We will first derive a slightly simpler variant of the method under the assumption that $u_{\text{inc}}(x, t)$ and $u(x, t)$ are spatially periodic on the interval B in the next section. The evaluation of the history part is discussed in section 3 and that of the local part in section 4.1, assuming the densities $\sigma_j(t)$ are known. The solution of the integro-differential equation to determine the density at each new time step is discussed in section 4.2 and the modifications needed for free-space scattering are described in section 4.4. Section 5 presents some theoretical analysis of stability and convergence for simple examples. Section 6 presents the results of a variety of numerical experiments. An appendix contains the proof of the main theorem.

Remark 1.2. *Fourier-based methods to overcome the history-dependence of time-dependent layer potentials were introduced in [11] in the context of the heat equation. The two key ideas from [11] are: (a) that high frequency spatial modes are rapidly damped by the heat kernel, so that a Fourier basis is highly effi-*

cient, and (b) that the coefficients of the spectral representation permit a simple evolution formula when marching from one time step to the next (exploiting the semigroup property of the solution operator).

For the wave equation, (b) also holds, but high frequency modes are not damped, so that additional ideas will be needed to make effective use of Fourier analysis.

Remark 1.3. A number of related approaches have been developed over the last few decades. For the Schrödinger equation, these include the use of contour deformation methods in Fourier space to attenuate high-frequency modes [12], methods that carefully filter outgoing waves at the boundary of a finite domain, permitting the use of the FFT on that domain [13–15]. Other methods worth noting that overcome the quadratic cost of history dependence include [16] and time-domain versions of the fast multipole for the heat and wave equations (see [17] and [1, 18], respectively).

2. Windowed Fourier projection in the periodic setting

To separate the issue of history dependence from that of imposing outgoing boundary conditions on a finite computational domain, we first assume that the incoming and scattered fields are both periodic on the domain $B = [-\pi, \pi]$. The scattered field BVP of interest is the wave equation (2) restricted to $x \in B$, with zero initial conditions, and continuity and jump conditions (4),(5) as before, plus periodicity imposed by matching Cauchy data:

$$u(-\pi, t) = u(\pi, t), \quad \partial_x u(-\pi, t) = \partial_x u(\pi, t), \quad t > 0. \quad (11)$$

As before, $u_{\text{inc}}(x, t) = f(x - t)$, which controls the driving functions $g_j(t)$ via (6). However, if u_{tot} is to be periodic, this requires that f be 2π -periodic.² To solve this BVP, u is represented as a periodic single-layer potential

$$u(x, t) = \sum_{j=1}^M \int_0^t G_p(x - x_j, t - \tau) \sigma_j(\tau) d\tau, \quad x \in \mathbb{R}, t > 0, \quad (12)$$

where $G_p(x, t)$ is the periodic 1D wave Green's function on B :

$$G_p(x, t) = \frac{1}{2} \sum_{m=-\infty}^{\infty} H(t - |x - 2\pi m|). \quad (13)$$

Rather than (10), imposing the jump relations now yields the system of Volterra integral equations

$$-\sigma_j(t) - \frac{\beta_j}{2} \sum_{l=1}^M \sum_{m=-\infty}^{\infty} \int_0^{t-|x_j-x_l-2\pi m|} \sigma_l(\tau) d\tau = g_j(t), \quad j = 1, \dots, M, t > 0, \quad (14)$$

which has the same history-dependence as before (in addition to the complexity of having a growing number of image contributions).

We could, however, replace G_p in (13) by its Fourier series representation:

$$G_p(x, t) = \frac{1}{2\pi} \left(t + \sum_{k \neq 0} \frac{\sin kt}{k} e^{-ikx} \right), \quad (15)$$

and seek the solution in the form

$$u(x, t) = \sum_{k=-\infty}^{\infty} u_k(t) e^{-ikx}. \quad (16)$$

Combining (12), (15) and (16) relates the Fourier coefficients $\{u_k\}$ to the densities $\{\sigma_j\}$:

$$u_k(t) = \int_0^t \frac{\sin k(t - \tau)}{k} S_k(\tau) d\tau, \quad k \in \mathbb{Z}, t > 0, \quad (17)$$

²Note that (2)–(5) with (11) also give a well-posed BVP with arbitrary driving functions $g_j(t)$.

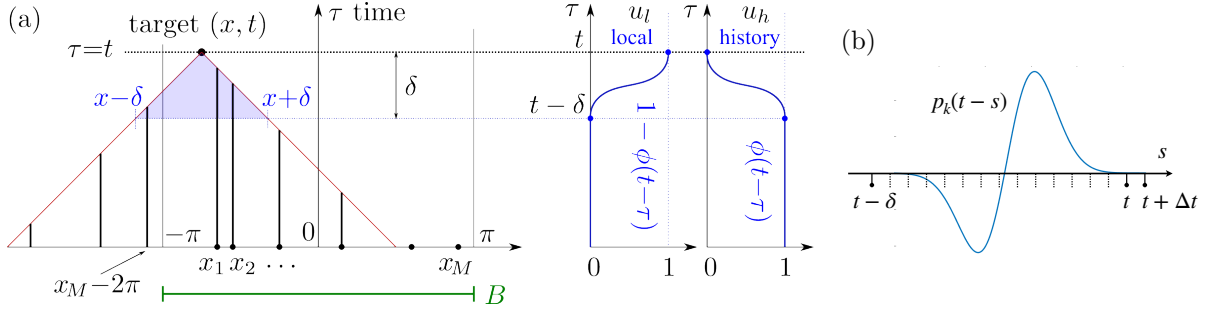


Figure 2: (a) Space-time diagram of density contributions $\sigma_j(\tau)$ (vertical lines) for evaluating $u(x, t)$ (left), showing the split via the window function ϕ into local and history components (right). The shaded triangle on the left shows the only spacetime region where densities contribute to u_L . (b) The weight functions p_k, q_k in (44), where k labels Fourier mode, vanish at times $s = t - \delta$ and $s = t + \Delta t$. Thus only known values of $\hat{\sigma}_k(\tau)$ in the recent past $t - \delta \leq \tau \leq 0$ are involved in computing $h_k(t), g_k(t)$ and, hence, $\alpha_k(t + \Delta t)$ (see text for details).

where we have introduced the k th spatial Fourier coefficient of the density distribution,

$$S_k(\tau) := \frac{1}{2\pi} \sum_{j=1}^M \sigma_j(\tau) e^{ikx_j}. \quad (18)$$

Remark 2.1. In (17) the $k = 0$ case is taken to mean the limit $\mathbb{R} \ni k \rightarrow 0$, so that $u_0(t) = \int_0^t (t - \tau) S_0(\tau) d\tau$. This limit is implied from now on for the $k = 0$ case when k appears in the denominator.

Note that, since the incident wave is smooth, and the BVP linear, the response of all the σ_j , and hence all of the S_k , are smooth in time. Furthermore, $S_k(\tau)$ “switches on” smoothly at $\tau = 0$ (i.e., it extends smoothly to the zero function in $\tau \leq 0$), because the support of the incident wave at $t = 0$ does not include any scatterers.

Unfortunately, the Fourier coefficients $u_k(t)$ in (17) are in general slowly decaying like $\mathcal{O}(1/k^2)$, since $u(x, t)$ is continuous but only piecewise-smooth (this low-order decay rate also follows directly from the discontinuous derivative at the upper limit in (17)). By analogy with the heat equation [11], one could try separating the scattered potential into a local part u_L plus a history part u_H :

$$u(x, t) = u_L(x, t) + u_H(x, t), \quad (19)$$

where a sharp transition at some time delay $\delta > 0$ into the past is used, so that

$$u_L(x, t) := \sum_{j=1}^M \int_{t-\delta}^t G_p(x - x_j, t - \tau) \sigma_j(\tau) d\tau, \quad (20)$$

$$u_H(x, t) := \sum_{j=1}^M \int_0^{t-\delta} G_p(x - x_j, t - \tau) \sigma_j(\tau) d\tau. \quad (21)$$

A simple calculation, however, shows that expanding only the history part in a Fourier series does not improve its convergence rate.

Here, we introduce the windowed Fourier projection method (WFP), an alternative decomposition which makes use of a smooth partition of unity based on a *blending function* $\phi(t)$ with $\phi(t) = 0$ for $t \leq 0$, and $\phi(t) = 1$ for $t \geq \delta$. We will later set the timescale parameter δ to be of order several time steps. Instead of (20) and (21), we define the local and history part as

$$u_L(x, t) := \sum_{j=1}^M \int_{t-\delta}^t G_p(x - x_j, t - \tau) [1 - \phi(t - \tau)] \sigma_j(\tau) d\tau, \quad (22)$$

$$u_H(x, t) := \sum_{j=1}^M \int_0^{t-\delta} G_p(x - x_j, t - \tau) \phi(t - \tau) \sigma_j(\tau) d\tau. \quad (23)$$

The local part u_L still represents the contribution from the densities $\{\sigma_j(t)\}$ windowed over the most

recent time interval (of length δ). In order to evaluate $u_L(x, t)$, we need only include those springs (or their periodic images) that lie within the interval $[x - \delta, x + \delta]$, since waves travel at unit speed. This interval and the windowing are sketched in Fig. 2(a). From now on we assume, for the sake of simplicity, that $\delta < \pi$ so that no more than one image source can lie in $[x - \delta, x + \delta]$.

Definition 1. For $x \in \mathbb{R}$, we denote by $\text{dist}(x, x_j)$ the distance from x to the nearest image of the source x_j :

$$\text{dist}(x, x_j) := \min_{m \in \mathbb{Z}} |x - (x_j + 2\pi m)|.$$

We denote by $\mathcal{N}_\delta(x)$ the set of indices of all points with images lying in $[x - \delta, x + \delta]$:

$$\mathcal{N}_\delta(x) := \{j = 1, \dots, M : \text{dist}(x, x_j) \leq \delta\}.$$

Using this definition, and recalling (13), the spatial form of G_p ,

$$u_L(x, t) = \frac{1}{2} \sum_{j \in \mathcal{N}_\delta(x)} \int_{t-\delta}^{t-\text{dist}(x, x_j)} [1 - \phi(t - \tau)] \sigma_j(\tau) d\tau. \quad (24)$$

An example where $\mathcal{N}_\delta(x)$ includes a periodically-wrapped source is sketched in Fig. 2(a).

For the history part u_H in (23), we use the Fourier representation

$$u_H(x, t) = \sum_{k=-\infty}^{\infty} \alpha_k(t) e^{-ikx}. \quad (25)$$

The coefficients $\{\alpha_k\}$ are driven by the full history of the spatial coefficients S_k of the density, recalling (18), except now with time windowing. That is,

$$\alpha_k(t) := \int_0^t \frac{\sin k(t - \tau)}{k} S_k(\tau) \phi(t - \tau) d\tau, \quad k \in \mathbb{Z}, t > 0, \quad (26)$$

which the reader should compare to (17). The key new feature is that $S_k(\tau)\phi(t - \tau)$ smoothly decays to zero at the upper limit $\tau = t$ because of the window function. Combined with the fact that S_k is already known to be smooth and smoothly vanishing at $\tau = 0$, this implies that for any fixed $t > 0$ the integral in (26) vanishes rapidly with respect to index $|k| \rightarrow \infty$: the Fourier series is spectrally convergent.

Making use of the local/history split, the coupled system of M Volterra integral equations for σ_j in (14) takes the form

$$-\sigma_j(t) - \frac{\beta_j}{2} \sum_{l \in \mathcal{N}_\delta(x_j)} \int_{t-\delta}^{t-\text{dist}(x_j, x_l)} \sigma_l(\tau) [1 - \phi(t - \tau)] d\tau - \frac{\beta_j}{2} \sum_{k=-\infty}^{\infty} \alpha_k(t) e^{-ikx_j} = g_j(t), \quad j = 1, \dots, M, t > 0, \quad (27)$$

where the α_k are given by (18) and (26). The Volterra system (27) with (18) and (26) is equivalent to the original integral equation (14) for the densities alone.

Numerically we will truncate the Fourier series to a maximum index K , i.e., we solve

$$-\sigma_j(t) - \frac{\beta_j}{2} \sum_{l \in \mathcal{N}_\delta(x_j)} \int_{t-\delta}^{t-\text{dist}(x_j, x_l)} \sigma_l(\tau) [1 - \phi(t - \tau)] d\tau - \frac{\beta_j}{2} \sum_{k=-K}^K \alpha_k(t) e^{-ikx_j} = g_j(t), \quad j = 1, \dots, M, t > 0, \quad (28)$$

where each of the α_k are given by (18) and (26) as above. The spectral convergence rate with respect to K of the truncation error is controlled by the smoothness of $\phi(t - \tau)$: if the window is less smooth than $S_k(\tau)$, then the α_k will decay excessively slowly as $|k| \rightarrow \infty$. The work in evaluating the Fourier sum in (28) scales like K , so reducing this work suggests a smoother window and a longer δ . Yet, the cost of the local evaluation (first sum in (28)) grows linearly with δ , suggesting that one push δ very small to reduce its work. These criteria are in conflict. An efficient scheme thus requires a ϕ that is *as smooth as possible for a given blending time* δ , and also chooses δ to balance the work of local and history parts.

We now formalize this intuition. While many windows (blending functions) ϕ are possible, in this paper we base it on the Kaiser–Bessel “bump” function $I_0(b\sqrt{1 - t^2})$ on $t \in [-1, 1]$, where $b > 0$ is a

shape parameter, and I_0 the modified Bessel function of order zero. This has the Fourier transform [19–21]

$$\int_{-1}^1 I_0(b\sqrt{1-t^2})e^{i\omega t} dt = 2 \operatorname{sinc} \sqrt{\omega^2 - b^2}, \quad \omega \in \mathbb{R}, \quad (29)$$

recalling the definition $\operatorname{sinc} z = \frac{\sin z}{z}$ for $z \neq 0$ and $\operatorname{sinc} 0 = 1$. For $|\omega| < b$ the right-hand side is exponentially large (nearly e^b/b at $\omega = 0$) because $\operatorname{sinc} iz = \frac{\sinh z}{z}$; in contrast for $|\omega| \geq b$ the right-hand side has magnitude at most 2. Thus the Fourier transform is exponentially (with respect to b) localized³ to the frequency interval $[-b, b]$. To create a blending function ϕ transitioning from 0 to 1 over the interval $[0, \delta]$, we need the antiderivative of a shifted and scaled bump,

$$\phi(t) = \int_0^t \phi'(\tau) d\tau, \quad t \in \mathbb{R}, \quad \text{where} \quad \phi'(t) = \begin{cases} \frac{b}{\delta \sinh b} I_0\left(b\sqrt{1 - (2t/\delta - 1)^2}\right), & 0 \leq t \leq \delta, \\ 0, & t < 0 \text{ or } t > \delta. \end{cases} \quad (30)$$

Although ϕ is actually nonsmooth at 0 and δ , having derivative jumps of size $\mathcal{O}(e^{-b})$, when one sets

$$b = \ln \frac{1}{\epsilon} \quad (31)$$

for some desired tolerance $\epsilon \ll 1$, then in practice ϕ is *numerically smooth* to this tolerance. Using as our definition of the Fourier transform

$$\hat{\phi}(\omega) := \int_{\mathbb{R}} \phi(t) e^{i\omega t} dt, \quad (32)$$

we have by rescaling (29) (or see (A.1)) that $\hat{\phi}(\omega)$ is of size $\mathcal{O}(\epsilon)$ for all $|\omega| \geq 2b/\delta$: its ϵ -support is $[-2b/\delta, 2b/\delta]$. We refer to $2b/\delta$ as the *cutoff frequency* or ϵ -bandlimit of the window, recalling the following.

Definition 2. We say a function $f \in L^2(\mathbb{R})$ is *bandlimited* with *bandlimit* $c > 0$ if

$$f(t) = \frac{1}{2\pi} \int_{-c}^c \hat{f}(\omega) e^{-i\omega t} d\omega, \quad t \in \mathbb{R}.$$

If the difference between left and right sides of the above has L^2 -norm $\mathcal{O}(\epsilon)$ relative to that of f , we say that f has ϵ -bandlimit c .

The principal analytic contribution of the present paper is the following theorem which bounds the tail of the Fourier series that has been truncated in (28), expressed by the error function

$$E_K(t) := \sum_{|k| > K} |\alpha_k(t)|, \quad t > 0. \quad (33)$$

This controls the *backward error* in the following sense. One may interpret the solution of (28) as the solution of the true Volterra equation (27) with perturbed data $\tilde{g}_j(t) = g_j(t) + \frac{\beta_j}{2} \sum_{|k| > K} \alpha_k(t) e^{-ikx_j}$ for each $j = 1, \dots, M$. Then $\beta_j E_K(t)/2$ is an upper bound on the residual $|\tilde{g}_j(t) - g_j(t)|$. For wave applications it is common to care about bandlimited excitation f in (1), and thus by linearity and time-invariance the solution and the densities must also have the same bandlimit, which we denote by K_0 in the following.

Theorem 1. Let σ_j have bandlimit K_0 and $\|\sigma_j\|_{L^2(\mathbb{R})} \leq C$ for each $j = 1, \dots, M$. Let the window ϕ be defined by (30) with shape parameter (31) and timescale $\delta > 0$. Let the Fourier series truncation frequency satisfy

$$K \geq K_0 + \frac{2b}{\delta}. \quad (34)$$

³Its degree of localization is close to optimal in the L^2 sense, and has the optimal exponential rate, since the function is very close to the prolate spheroidal wavefunction of order zero [22, 23].

Then the norm of the error function (33) over a finite simulation time $t \in (0, T)$ has the bound

$$\|E_K\|_{L^2(0,T)} \leq 2\pi^2 TMC \frac{b}{\delta \sinh b} = \mathcal{O}\left(\epsilon \log \frac{1}{\epsilon}\right) \quad \text{as } \epsilon \rightarrow 0. \quad (35)$$

We defer its proof to [Appendix A](#). The big-O statement in (35) simply applies (31). We thus expect almost exponential convergence of the residual with respect to b (recalling $\sinh b \sim e^b/2$), as long as the densities are (numerically) bandlimited and the bandwidth sum condition (34) holds. An interpretation of the latter is that the windowing (the pointwise multiplication by ϕ in (26)) enlarges the density bandlimit K_0 by the window ϵ -bandlimit $2b/\delta$. The sinusoidal wave propagator term in (26) then converts this temporal ϵ -bandlimit to an equal spatial one, so that Fourier series truncation to this bandlimit induces errors close to $\mathcal{O}(\epsilon)$. From a physical perspective, an incident field with bandlimit K_0 cannot scatter “propagating” spatial frequency modes of the form e^{ikx} in the actual solution with $|k| > K_0$. In essence, the singular structure near the springs is resolved by the local part, while the window function filters out the “non-propagating” components from the history part.

Remark 2.2 (Choice of Fourier truncation K). *Choosing an equality in (34), we denote the fraction of the resulting numerical bandlimit K which is “lost” to windowing by γ , so that $2b/\delta = \gamma K$ while $K = K_0/(1 - \gamma)$. The sharper the window (smaller the timescale δ), the less work associated with the local part, but the greater the effective bandlimit K . Thus, the selection of the parameter δ can be used to balance the workload between the local and history parts. In the present paper, we typically fix $\gamma = 1/2$, so that $K = 2K_0$. In turn, K_0 may be chosen as the ϵ -bandlimit of the incident signal f .*

We end the section by mentioning technical limitations in [Theorem 1](#). 1) We were unable to state a hypothesis involving a bandlimit on f or even g_j , and instead made it on σ_j (a stronger condition). We expect (and observe) this to hold to numerical accuracy, but note that a strict bandlimit is probably not the right condition for a broader analysis. For instance, bandlimited functions are entire, and thus identically zero if they vanish for $t < 0$: causality and being bandlimited are incompatible. 2) The hypothesis that the densities be in $L^2(\mathbb{R})$ most likely does not hold for densities solving the *periodic* BVP (2)–(5) plus (11). This is because the scattered wave continues to bounce around B for all time. However, in the more applicable free-space case the densities decay back down to zero making the condition plausible. We are unable at this time to weaken this condition to something more local in time, again because the definition of bandlimited involves all of \mathbb{R} . We leave a refined analysis for future work.

3. Evaluation of the history part using recurrences

The reason we propose a Fourier representation for the history is that, while the Fourier coefficients themselves are fully history-dependent, they can be updated recursively. A direct computation using (26) shows that

$$\alpha_k''(t) + k^2 \alpha_k(t) = F_k(t), \quad \text{with driving} \quad F_k(t) := \int_{t-\delta}^t \Psi_k(t - \tau) S_k(\tau) d\tau, \quad (36)$$

given in terms of the blending “influence kernel”

$$\Psi_k(\tau) := 2 \cos k\tau \phi'(\tau) + \frac{\sin k\tau}{k} \phi''(\tau), \quad \tau \in \mathbb{R}, \quad (37)$$

whose support is $[0, \delta]$. Thus the k th coefficient obeys a 2nd-order linear ODE driven by F_k , a weighted integral of S_k over the most recent time interval of length δ . It is useful to rewrite (36) as the linear 1st-order system

$$\partial_t \begin{bmatrix} \alpha_k(t) \\ \alpha_k'(t) \end{bmatrix} = \begin{bmatrix} 0 & 1 \\ -k^2 & 0 \end{bmatrix} \begin{bmatrix} \alpha_k(t) \\ \alpha_k'(t) \end{bmatrix} + \begin{bmatrix} 0 \\ F_k(t) \end{bmatrix}, \quad t > 0. \quad (38)$$

For each $k \in \mathbb{Z}$, the matrix which propagates the homogeneous system over a time t is easily seen to be

$$\begin{bmatrix} \cos kt & \frac{\sin kt}{k} \\ -k \sin kt & \cos kt \end{bmatrix}. \quad (39)$$

The Duhamel principle then proves the following.

Lemma 3.1. *Let Δt denote a time step. Then the Fourier coefficients $\alpha_k(t)$ satisfy the evolution formulae*

$$\begin{aligned}\alpha_k(t + \Delta t) &= \alpha_k(t) \cos k\Delta t + \alpha'_k(t) \frac{\sin k\Delta t}{k} + h_k(t), \\ \alpha'_k(t + \Delta t) &= -k\alpha_k(t) \sin k\Delta t + \alpha'_k(t) \cos k\Delta t + g_k(t),\end{aligned}\tag{40}$$

where, recalling the definition of F_k in (36) and (37),

$$h_k(t) := \int_t^{t+\Delta t} \frac{\sin k(t + \Delta t - \tau)}{k} F_k(\tau) d\tau, \quad g_k(t) := \int_t^{t+\Delta t} \cos k(t + \Delta t - \tau) F_k(\tau) d\tau.\tag{41}$$

The preceding lemma yields exact one-step recurrences for α_k , and α'_k . The driving updates, $h_k(t)$ and $g_k(t)$, however, need to be computed numerically. From (36) we have

$$\begin{aligned}h_k(t) &= \int_t^{t+\Delta t} \frac{\sin k(t + \Delta t - \tau)}{k} \left\{ \int_{\tau-\delta}^{\tau} \Psi_k(\tau - s) S_k(s) ds \right\} d\tau, \\ g_k(t) &= \int_t^{t+\Delta t} \cos k(t + \Delta t - \tau) \left\{ \int_{\tau-\delta}^{\tau} \Psi_k(\tau - s) S_k(s) ds \right\} d\tau.\end{aligned}\tag{42}$$

Because Ψ_k vanishes outside $[0, \delta]$, one can change the limits of the inner integrals to $[t - \delta, t + \Delta t]$, then swap the order of integration to yield

$$h_k(t) = \int_{t-\delta}^{t+\Delta t} p_k(t - s) S_k(s) ds, \quad g_k(t) = \int_{t-\delta}^{t+\Delta t} q_k(t - s) S_k(s) ds,\tag{43}$$

where the ‘‘one timestep integrated’’ influence kernels are

$$\begin{aligned}p_k(t - s) &:= \int_0^{\Delta t} \frac{\sin k(\Delta t - \mu)}{k} \Psi_k(t - s + \mu) d\mu, \\ q_k(t - s) &:= \int_0^{\Delta t} \cos k(\Delta t - \mu) \Psi_k(t - s + \mu) d\mu.\end{aligned}\tag{44}$$

Recalling from (30) that Ψ_k is smooth on \mathbb{R} apart from discontinuities of size $\mathcal{O}(\epsilon)$ at either end of its support $[0, \delta]$, we see that p_k and q_k vanish at the endpoints $t - s = -\Delta t$ and $t - s = \delta$, and are smooth apart from derivative discontinuities of size $\mathcal{O}(\epsilon)$ (see Fig. 2(b)). As a result, the trapezoidal rule [24] is *spectrally accurate* (up to $\mathcal{O}(\epsilon)$) for approximating the integrals in (43), and we thus use the available uniform time grid, with time step Δt , as its quadrature nodes. Specifically, letting n be the index of the current time step, so that $t = n\Delta t$, we employ the discrete formulae

$$\begin{aligned}h_k(n\Delta t) &\approx \Delta t \sum_{m=0}^{W-1} p_k(m\Delta t) S_k((n - m)\Delta t), \\ g_k(n\Delta t) &\approx \Delta t \sum_{m=0}^{W-1} q_k(m\Delta t) S_k((n - m)\Delta t),\end{aligned}\tag{45}$$

where we chose

$$\delta = W\Delta t\tag{46}$$

for some integer W setting the number of time steps in the window width. These explicit formulae, involving only known data on the grid, are inserted into (40) to time-step the α_k and α'_k coefficients. In the above, the needed terms $p_k(m\Delta t)$ and $q_k(m\Delta t)$ for $m = 0, \dots, W - 1$ are easily approximated to negligible error by applying a N_g -node Gauss–Legendre quadrature rule to the integrals (44).

3.1. Parameter choices and a fast algorithm for the history part

The windowed Fourier projection and the timestepping of its history part described so far is a spectral method. Recall that K is the highest frequency component kept in the truncated Fourier series, so that

there are a total of $N_F = 2K + 1$ modes. A grid with time step Δt cannot discretize signals beyond a bandlimit of $\pi/\Delta t$ (i.e., the signal with alternating signs on the grid) without aliasing; this is the *Nyquist frequency* [25, §4.6]. This gives an upper bound on K (the same upper bound results by requiring that the trapezoid quadrature be accurate out to the maximum bandlimit $2K$ of the integrands in (43)). Making K larger than this is waste. Thus, we connect the spatial and temporal discretizations via

$$K = \frac{\pi}{\Delta t}, \quad (47)$$

based on whatever Δt is chosen for accuracy and efficiency reasons. We now see that $W = \mathcal{O}(1)$, the window timescale in time steps, as follows. Remark 2.2 stated that the window ϵ -bandlimit is $2b/\delta = \gamma K$, and combining with (47) and (46) gives

$$W = \frac{2b}{\pi\gamma} = \frac{2}{\pi\gamma} \log \frac{1}{\epsilon}.$$

For instance, $\epsilon = 10^{-12}$ and $\gamma = 1/2$ gives $W \approx 35$, a setting that we typically use in later experiments.

We now turn to computational cost. Computing the values $p_k(m\Delta t)$, $q_k(m\Delta t)$ for $m = 1, \dots, W$ requires $\mathcal{O}(KW N_g)$ work, where N_g denotes the number of Gauss–Legendre nodes used for quadrature of (44). Since W and N_g are of order 1, this precomputation is effectively $\mathcal{O}(K)$ work and is negligible.

At the n th time step, computing $h_k(n\Delta t)$ and $g_k(n\Delta t)$ via (45) involves two steps. First we must compute $S_k(n\Delta t)$ according to (18), repeated here:

$$S_k(n\Delta t) := \frac{1}{2\pi} \sum_{j=1}^M \sigma_j(n\Delta t) e^{ikx_j}, \quad k = -K, -K + 1, \dots, K.$$

A naive calculation would require $\mathcal{O}(MK)$ work. However, the form of the exponential sum is that of a nonuniform FFT of type 1 [26–28], so the set of values $\{S_k(n\Delta t)\}_{|k| \leq K}$ can be approximately computed together to relative error ϵ in $\mathcal{O}(M \log(1/\epsilon) + K \log K)$ time. These values for the previous W time steps must be stored to compute (45), needing $\mathcal{O}(WK)$ storage. Then, applying (40) costs only $\mathcal{O}(K)$. Thus, obtaining the α_k coefficients of the history part (25) at each time step requires $\mathcal{O}(M + K \log K)$ work.

The other history-related task each time step is to evaluate the history representation back at the scatterers, for the α -dependent term in (28). This takes the form of a nonuniform FFT of type 2; it is the adjoint of the type 1 and requires the same computational effort. If other solution evaluation points are needed, they can be appended to the list of scatterers in this step, with a linear cost. In summary, handling the history part for the Volterra equation (28) requires $\mathcal{O}(M + K \log K)$ work per time step.

4. Evaluation of the local part, time marching, and free space boundary conditions

In this section we describe the remaining ingredients needed to efficiently time march a fully discrete version of the Volterra integral equation system (28), and to change the boundary conditions from periodic to free-space.

4.1. Approximation of the local part via p th-order density interpolation

Here we tackle the local part of the single layer potential, namely the 2nd term in (28), needed to advance from time $t_n = n\Delta t$ to $t_{n+1} = (n+1)\Delta t$. We denote the target point by x ; this could be the j th scatterer x_j , or another point at which the scattered field $u(x, t_{n+1})$ is desired. We distinguish “nearby” sources with $\text{dist}(x, x_j) < \Delta t$ from the remaining more numerous “intermediate” distance sources with $\Delta t \leq \text{dist}(x, x_j) < \delta$. Recalling Definition 1, the nearby indices are $\mathcal{N}_{\Delta t}(x)$, while we denote the intermediate indices by $\mathcal{I}_\delta(x) := \mathcal{N}_\delta(x) \setminus \mathcal{N}_{\Delta t}(x)$. From (24), using l as the source index, we have

$$u_L(x, t_{n+1}) = \sum_{l \in \mathcal{N}_{\Delta t}(x)} \int_{t_{n+1}-\delta}^{t_{n+1}-\text{dist}(x, x_l)} [1 - \phi(t_{n+1}-\tau)] \frac{\sigma_l(\tau)}{2} d\tau + \sum_{l \in \mathcal{C}_\delta(x)} \int_{t_{n+1}-\delta}^{t_{n+1}-\text{dist}(x, x_l)} [1 - \phi(t_{n+1}-\tau)] \frac{\sigma_l(\tau)}{2} d\tau. \quad (48)$$

The reason for distinguishing the two sets of source points is that computing the integrals for $l \in \mathcal{N}_{\Delta t}(x)$ will involve the unknown $\sigma_l(t_{n+1})$ (see Fig. 3.1 middle and right panels), while the integrals for $l \in \mathcal{C}_\delta(x)$ use only known values of the density σ_l at time t_n or earlier (Fig. 3.1 left panel).

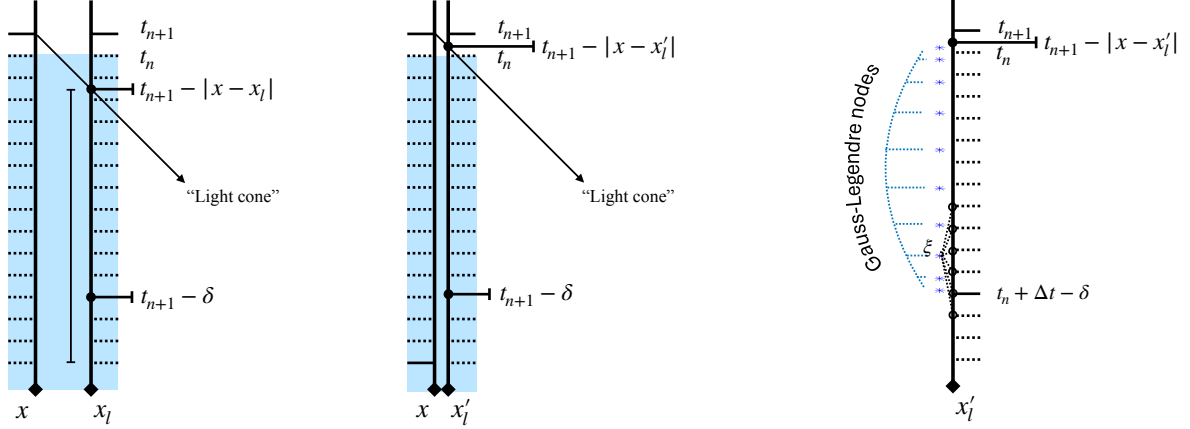


Figure 3: Left side: source point x_l has “intermediate” distance from x , i.e., between Δt and δ , so the characteristic (light cone) emanating from spacetime point (x, t_{n+1}) hits x_l before t_n . Thus, the integrand over the interval $[t_{n+1} - \delta, t_{n+1} - |x - x_l|]$ can be computed from known values (indicated by the shaded region) of the density $\sigma_l(t)$. Middle: the source point x'_l is “nearby” (closer than Δt), so that the light cone intersects x'_l after the time t_n (outside the shaded region), and interpolation requires the unknown density $\sigma_l(t_{n+1})$. Right: quadrature nodes ξ_i for the integration domain $[t_{n+1} - \delta, t_{n+1} - \text{dist}(x, x_l)]$, in the nearby case. The small fan of dotted lines indicates degree- $(p - 1)$ local interpolation to a single node ξ from the p nearest regular grid values.

Each integral in the sums in (48) is approximated by a single Gauss–Legendre quadrature rule over their domain, with the off-grid density values at these quadrature nodes approximated via local degree- $(p - 1)$ polynomial interpolation from the p nearest known regular grid values. Specifically, consider the term involving either a nearby or intermediate source x_l , and let $\{\xi_i\}_{i=1}^{N_L}$ be the Gauss–Legendre nodes and $\{w_i\}_{i=1}^{N_L}$ the corresponding weights for the interval $\tau \in [t_{n+1} - \delta, t_{n+1} - \text{dist}(x, x_l)]$. The interpolant evaluated at one of these nodes ξ depends linearly on the grid values $\sigma_l^n := \sigma_l(t_n)$, as follows:

$$\tilde{\sigma}_l(\xi) = \sum_{m \in \mathcal{I}(\xi)} v_m(\xi) \sigma_l^{n+1-m}, \quad (49)$$

where $\mathcal{I}(\xi)$ is the set of indices of the p nearest available points to ξ from the grid $\{t_{n+1-m}\}_{m=m_{\min}}^{m_{\max}}$. See Fig. 3.1, right panel. Here $m_{\max} = W + \lceil p/2 \rceil$, to allow for interpolation to target times the furthest in the past, t_{n+1-W} . The lower allowable index is $m_{\min} = 0$ (accessing t_{n+1}) if x_l is a nearby source, or $m_{\min} = 1$ if an intermediate distance source. The interpolation weights v_m are computed by standard barycentric Lagrange interpolation [25, §4.2.3]. We expect an accuracy $\mathcal{O}((\Delta t)^p)$ for this p -node polynomial interpolant.

Each integral term in (48) is then approximated as

$$\int_{t_{n+1}-\delta}^{t_{n+1}-\text{dist}(x, x_l)} [1 - \phi(t_{n+1} - \tau)] \sigma_l(\tau) d\tau \approx \sum_{i=1}^{N_L} w_i [1 - \phi(t_{n+1} - \xi_i)] \tilde{\sigma}_l(\xi_i) \approx \sum_{m_{\min}}^{m_{\max}} Q_m(\text{dist}(x, x_l)) \sigma_l^{n+1-m}.$$

The formula for the weights is, from (49),

$$Q_m(\text{dist}(x, x_l)) = \sum_{i: m \in \mathcal{I}(\xi_i)} w_i [1 - \phi(t_{n+1} - \xi_i)] v_m(\xi_i), \quad m = m_{\min}, m_{\min} + 1, \dots, m_{\max},$$

recalling that the nodes ξ_i and weights w_i themselves depend on $\text{dist}(x, x_l)$. If $\text{dist}(x, x_l) > \delta$, we define all Q_m as zero.

The above holds for local evaluation at an arbitrary target $x \in B$. For the specific case of $x = x_j$ we will abbreviate $Q_{jlm}^N := Q_m(\text{dist}(x_j, x_l))$ when x_l is nearby, while $Q_{jlm}^C := Q_m(\text{dist}(x_j, x_l))$ when x_l is at intermediate distance. The complete formulae for Q_m incorporating barycentric weights are cumbersome and available in the accompanying software [29].

4.2. The fast method for time marching

Let us abbreviate $g_j^n := g_j(t_n)$, and $\alpha_k^n = \alpha_k(t_n)$, $|k| < K$, for the time steps $t_n = n\Delta t$, $n = 0, 1, \dots, N_t$. A fully discrete version of the integral equation (28) is, setting $t = t_{n+1}$ and applying the above local evaluation quadratures,

$$-\sigma_j^{n+1} - \frac{\beta_j}{2} \sum_{l \in \mathcal{N}_{\Delta t}(x_j)} \sum_{m=0}^{m_{\max}} Q_{jlm}^{\mathcal{N}} \sigma_l^{n+1-m} - \frac{\beta_j}{2} \sum_{l \in \mathcal{C}_{\delta}(x_j)} \sum_{m=1}^{m_{\max}} Q_{jlm}^{\mathcal{C}} \sigma_l^{n+1-m} - \frac{\beta_j}{2} \sum_{k=-K}^K \alpha_k^{n+1} e^{-ikx_j} = g_j^{n+1}, \quad (50)$$

for $j = 1, \dots, M$. Notice that the nearby (first) sum involves σ_l^{n+1} , and thus is an ‘‘implicit’’ formula, while the intermediate (second) sum plus the history part (since the α_l^{n+1} update only needs densities at t^n or earlier), are ‘‘explicit’’ terms. This yields an implicit marching scheme that requires the solution of a sparse, banded linear system at each time step, with the number of non-zeros in the j th row determined by the number of nearby points, namely $|\mathcal{N}_{\Delta t}(x_j)|$. (If no scatterers are within Δt of each other, the system of equations is diagonal.)

Defining at the n th time step the vectors of densities $\boldsymbol{\sigma}^n := [\sigma_1^n, \dots, \sigma_M^n]$, right-hand sides $\boldsymbol{g}^n := [g_1^n, \dots, g_M^n]$, and history coefficients $\boldsymbol{\alpha}^n := [\alpha_{-K}^n, \dots, \alpha_K^n]$, it is easy to see that (50) can be written as a linear system of the form

$$-(I + S)\boldsymbol{\sigma}^{n+1} = \boldsymbol{g}^{n+1} + \sum_{m=1}^{m_{\max}} C^{(m)} \boldsymbol{\sigma}^{n+1-m} + E\boldsymbol{\alpha}^{n+1}, \quad (51)$$

where $\boldsymbol{\alpha}^{n+1}$ is obtained via the history update equations (40) and (45), implemented via the type 1 NUFFT as in Section 3; these only involve $\boldsymbol{\sigma}^{n+1-m}$ for $m = 1, \dots, W$, and $\boldsymbol{\alpha}^n$ and $\boldsymbol{\alpha}^{n'}$. Thus all of the terms on the right-hand side of (51) are known. The system matrix has the following structure: I is the $M \times M$ identity matrix, while S is a sparse matrix with non-zero entries $S_{jl} = \frac{\beta_j}{2} Q_{jil}^{\mathcal{N}}$ whenever $\text{dist}(x_j, x_l) < \Delta t$, for $j, l = 1, \dots, M$. Each matrix $C^{(m)} \in \mathbb{R}^{M \times M}$ is sparse with non-zero entries

$$C_{jl}^{(m)} = \begin{cases} (\beta_j/2) Q_{jlm}^{\mathcal{N}}, & \text{dist}(x_j, x_l) < \Delta t, \\ (\beta_j/2) Q_{jlm}^{\mathcal{C}}, & \Delta t \leq \text{dist}(x_j, x_l) < \delta, \end{cases} \quad \text{for } j, l \in 1, \dots, M.$$

E represents the discrete nonuniform Fourier transform matrix of size $M \times (2K + 1)$ with entries

$$E_{jk} = \frac{\beta_j}{2} e^{-ikx_j}, \quad (52)$$

and can be applied rapidly using the type 2 NUFFT, as discussed at the end of Section 3.

We expect the error for one time step to scale like the interpolation order p plus one, since the local integral has an extra factor Δt . The history part we expect to be spectrally accurate, with parameters chosen for a fixed tolerance ϵ . Since there are $N_t = \mathcal{O}(1/\Delta t)$ time steps to reach a fixed final time T , the overall error we expect to be at least $\mathcal{O}((\Delta t)^p + \epsilon)$.

4.3. Computational complexity of the full method

From now on let $M_{\text{typ}} := (1/M) \sum_{j=1}^M |\mathcal{N}_{\delta}(x_j)|$ denote the mean number of neighbors involved in the local part evaluation of a scatterer. If the Δt needed to achieve accuracy for the given incident signal f is too large, we recommend decreasing Δt for efficiency reasons so that M_{typ} is $\mathcal{O}(1)$. In practice we find that M_{typ} of order 10^2 balances history and local costs. Precomputing all local quadrature weights $Q_{jlm}^{\mathcal{N}}$ and $Q_{jlm}^{\mathcal{C}}$ is a one-time cost of $\mathcal{O}(N_L p M_{\text{typ}} M) = \mathcal{O}(M)$, with a large prefactor (however we will see that its cost is less than 10^2 time-steps). By a convergence study we found that $N_L = W$ is sufficient. The cost of evaluating the local part $u_L(x_j, t_{n+1})$ at a single target is $\mathcal{O}(W M_{\text{typ}})$, thus its total cost per time step is $\mathcal{O}(M)$. In practice we reduce its prefactor by applying the stack of $C^{(m)}$ matrices via a single sparse matrix-vector multiply. The storage cost for the densities over the needed recent past is $M m_{\max} = M(W + \lceil \frac{p}{2} \rceil)$ complex numbers. We also store the recent W vectors of $\{S_k\}_{k=-K}^K$ to avoid them having to be recomputed. This means that there is a one type 1 and one type 2 NUFFT, a cost $\mathcal{O}(M + K \log K)$, each time step.

As for the integral equation itself, to obtain $\boldsymbol{\sigma}^{n+1}$ requires solving (51) each time step. This requires $\mathcal{O}(M)$ work per time step since S is banded with a bandwidth of $\max_j |\mathcal{N}_{\Delta t}(x_j)|$, which is $\mathcal{O}(M_{\text{typ}})$ if

the springs are more or less uniformly distributed. We accelerate the solve by sparse LU factorization of $I + S$ once and for all.

Note that the condition $M_{\text{typ}} = \mathcal{O}(1)$ means that $\Delta t = \mathcal{O}(1/M)$, and recalling (47), $K = \mathcal{O}(M)$. Thus the overall cost per time step may be summarized as $\mathcal{O}(M + K \log K) = \mathcal{O}(M \log M)$, giving a total solution cost over a fixed interval $(0, T)$ of $\mathcal{O}(N_t M \log M) = \mathcal{O}(M^2 \log M)$. This contrasts with $\mathcal{O}(N_t^2 M^2)$ for naive time-stepping of the Volterra equation.

4.4. Imposing free-space boundary conditions via outgoing windowing

Imposing radiation boundary conditions (RBCs) for the scattered solution of the wave equation in the 1D box B is easy compared to the higher dimensional case, because they are *local* in space and time, namely $\partial_x u \pm \partial_t u = 0$ at $x = \pm\pi$ respectively. (For some of the recent literature on the higher-dimensional case see [14, 15, 30, 31].) In the spirit of the presented WFP method, we present a simple—but we believe new—spectrally accurate method which acts on the history part. At certain time steps, a fixed matrix $P \in \mathbb{C}^{2N_F \times 2N_F}$ modifies the coefficient vectors $\boldsymbol{\alpha} := \{\alpha_k\}_{k=-K}^K$ and $\boldsymbol{\alpha}' := \{\alpha'_k\}_{k=-K}^K$ via

$$\begin{bmatrix} \boldsymbol{\alpha} \\ \boldsymbol{\alpha}' \end{bmatrix} \leftarrow P \begin{bmatrix} \boldsymbol{\alpha} \\ \boldsymbol{\alpha}' \end{bmatrix}.$$

We will see that this must be performed every few time steps.

The action of P is best described as the composition of three steps. Step 1 takes the FFT of the vectors $\boldsymbol{\alpha}$ and $\boldsymbol{\alpha}'$ to get values on a spatial grid. It is slightly neater (and incurs negligible error) to first discard the highest frequency $k = K$, so that the FFTs have length $n = 2K$. The FFT of the (FFT-shifted) vector $\boldsymbol{\alpha}$ then outputs the grid of values $u_H(0), u_H(h), \dots, u_H((K-1)h), u_H(-Kh), u_H((-K+1)h), \dots, u_H(-h)$, where the grid spacing is $h = \Delta t = 2\pi/n$, recalling (47). We will drop the H (history) subscript. The FFT of $\boldsymbol{\alpha}'$ generates a similar grid but for the function $v := \partial_t u$.

For step 2 we now interpret the window ϕ given by (30), with the same shape parameter b chosen for tolerance ϵ as in (31), as a spatial rather than temporal blending function. The blending occurs from 0 up to 1 over W gridpoints. Consider imposing a right-going condition at the right endpoint at $x = \pi$. The (zero-indexed) index set $I = \{K-2W, K-2W+1, \dots, K-1\}$ in the u grid from step 1 corresponds to the interval $R = [\pi - 2\delta, \pi)$ where modification will occur. At $x = ih$ for each $i \in I$ we compute “rolled-off” grid values

$$\tilde{u}(x) = \phi(\pi - \delta - x)u(x), \tag{53}$$

$$\tilde{v}(x) = \phi'(\pi - \delta - x)u(x) + \phi(\pi - \delta - x)v(x). \tag{54}$$

The window $\phi(\pi - \delta - x)$ starts at 1 at the left end of the region R , drops to 0 by the middle of R , and stays zero until its right end. Thus \tilde{u} is a version of u rolled off to zero over the distance δ . If u and $v = \partial_t u$ already describe a right-going wave in R , then (54) sets \tilde{v} to have the right-going condition to match \tilde{u} :

$$\tilde{v}(x) = \partial_t \tilde{u}(x) = -\partial_x \tilde{u}(x) = -\partial_x (\phi(\pi - \delta - x)u(x)) = \phi'(\pi - \delta - x)u(x) - \phi(\pi - \delta - x)\partial_x u(x),$$

and finally the right-going hypothesis $\partial_x u = -\partial_t u$ justifies (54). The u and v values at the grid point indices I are now replaced with \tilde{u} and \tilde{v} . A reflection of Step 2 is similarly applied on the left end, for which the index set is $I = \{K, K+1, \dots, K+2W-1\}$.

Step 3 applies inverse FFTs to the resulting u and v grids to give the new coefficient vectors $\boldsymbol{\alpha}$ and $\boldsymbol{\alpha}'$, appending by zero for the $k = K$ entry. This completes the action of P . The MATLAB implementation is about 10 lines of code (see `alphaRBCproj.m` in [29]).

We now explain the requirement on the period Δt_{proj} between such RBC “projections.”⁴ The new coefficients represent a field unchanged in $|x| < \pi - 2\delta$, but rolled off to zero and outgoing in $|x| \in [\pi - 2\delta, \pi]$. One can wait up to 2δ before the support of the rolled off wave wraps around the periodic domain and hits $|x| = \pi - \delta$, where it would start to break the hypothesis that (u, v) represent outgoing waves in $|x| \in [\pi - 2\delta, \pi - \delta]$. Thus $\Delta t_{\text{proj}} \leq 2\delta = 2W\Delta t$. However, repeating before δ would cause repeated window multiplication on the same piece of traveling wave, unnecessarily growing its spectral bandwidth and perhaps causing aliasing. In summary, any Δt_{proj} between W and $2W$ time steps is

⁴We use quotes here since $P^2 \neq P$, associated with ϕ having a continuous transition from 0 to 1.

valid. An increase in bandwidth by γK is expected (Remark 2.2); however, this only affects waves that will shortly be zeroed out, and empirically we find errors $\mathcal{O}(\epsilon)$ matching the window tolerance.

To ensure that no local evaluation affects either rolled-off region, the scatterers must all reside in a computational domain $\Omega := [-\pi + 3\delta, \pi - 3\delta]$, only slightly smaller than the periodic box $B = [-\pi, \pi]$.

The cost of this RBC is four FFTs of length N_F , performed every $\mathcal{O}(W)$ time steps, negligible compared to the integral equation cost. The complexity of the free-space method is thus the same as that of the spatially periodic method.

5. Stability and convergence for model problems

Here we prove some results for p th-order interpolatory marching as in Sections 4.1–4.2, applied to (10), the original system of Volterra integral equations involving the free-space Green’s function. This is the relevant question, because the WFP (local/history split), RBC, and Gauss–Legendre quadratures together approximate (10) to spectral accuracy (their errors that can easily be pushed down to close to machine precision).

We study discretizations coming from 1st- or 2nd-order density interpolants, and the case of $M = 1$ and $M = 2$ springs (scatterers); we believe that this covers the main issues arising with nearby or well-separated springs. It also serves to illustrate the time stepping schemes in simple cases. Since we seek stability results that do not allow exponential growth in the prefactor, we employ direct methods as in [32, §7.5]. The stability proofs already involve subtleties, so we defer more generality to future work. We end with a 2nd-order convergence proof for two springs in the style of [32, Thm 7.2], which in contrast will involve an exponentially growing prefactor.

5.1. Stability for one spring ($M = 1$)

This simple case serves to recap the difference equation method [32, §7.5]. With one spring (10) is a scalar Volterra equation with constant kernel, so we drop the j index and have

$$-\sigma(t) - \frac{\beta}{2} \int_0^t \sigma(\tau) d\tau = g(t),$$

of course equivalent to a first-order ODE IVP. For an order $p = 1$ interpolant we use in each time step the density at the start of that time step:

$$\sigma(\tau) \approx \sigma^\nu, \quad t_\nu \leq \tau < t_{\nu+1}, \quad \nu = 1, 2, \dots, N_t - 1.$$

Substituting this into the above gives, in terms of the scaled time-step $\alpha := \frac{\beta \Delta t}{2}$, the $\mathcal{O}(\Delta t)$ accurate explicit time step method

$$\sigma^{n+1} + \alpha \sum_{\nu \leq n} \sigma^\nu = -g^{n+1}.$$

Subtracting the equation where $n+1$ is replaced by n shows that the density obeys the difference equation

$$\sigma^{n+1} + (\alpha - 1)\sigma^n = -\Delta g^{n+1}$$

driven by $\Delta g^{n+1} := g^{n+1} - g^n$. Its characteristic equation is $p(z) := z + \alpha - 1 = 0$, and the difference equation is stable if all solutions (roots of p) have $|z| < 1$ [32, §7.5]. The latter would insure that all homogeneous solutions are exponentially decaying. This root condition holds whenever $\alpha \in (0, 2)$, thus for all $\Delta t < 4/\beta$. (This is the same bound as the forward Euler method for the corresponding first-order ODE.)

Instead, for $p = 2$, substituting the $\mathcal{O}(\Delta t^2)$ accurate piecewise-linear interpolant

$$\sigma(\tau) \approx \frac{t_{\nu+1} - \tau}{\Delta t} \sigma^\nu + \frac{\tau - t_\nu}{\Delta t} \sigma^{\nu+1}, \quad t_\nu \leq \tau < t_{\nu+1}, \quad (55)$$

gives the implicit method (analogous to an order-2 linear multistep method or LMM),

$$\sigma^{n+1} + \frac{\alpha}{2} \sigma^{n+1} + \alpha \sum_{\nu \leq n} \sigma^\nu = g^{n+1}.$$

Again subtracting the $n + 1$ and n cases gives the difference equation $(1 + \alpha/2)\sigma^{n+1} - (1 - \alpha/2)\sigma^n = -\Delta g^{n+1}$, whose characteristic polynomial has the single root $z = (1 - \alpha/2)/(1 + \alpha/2)$, inside the unit circle for all $\alpha > 0$. The method is thus unconditionally stable (analogous to the A-stability of the Crank–Nicholson method for the equivalent ODE [32, p. 111]).

5.2. Stability for two springs ($M = 2$)

Let the spring separation be $L := |x_2 - x_1|$. The coupled Volterra equations (10) are then, for $t > 0$,

$$\sigma_1(t) + \frac{\beta}{2} \int_0^t \sigma_1(\tau) d\tau + \frac{\beta}{2} \int_0^{t-L} \sigma_2(\tau) d\tau = -g_1(t), \quad (56)$$

$$\sigma_2(t) + \frac{\beta}{2} \int_0^{t-L} \sigma_1(\tau) d\tau + \frac{\beta}{2} \int_0^t \sigma_2(\tau) d\tau = -g_2(t), \quad (57)$$

where we note the symmetry that the second equation is the first with the labels $j = 1$ and 2 swapped. The following proves that 1st-order time-stepping is stable up to a maximum Δt , independent of how large L is.

Theorem 5.1 (Explicit first-order time-stepping for two springs at arbitrary separation).

Let $\Delta t \in (0, 2/\beta)$, and let $x_1, x_2 \in \mathbb{R}$. Then the discrete Volterra equations arising by applying the piecewise-constant ($p = 1$, i.e., 1st-order) interpolant (5.1) to (56)–(57) and integrating exactly are stable, in the following sense: if the right-hand side data $g_{1,2}^n$ are zero for all sufficiently large n , the densities $\sigma_{1,2}^n$ remain uniformly bounded, and in fact decay exponentially to at worst a constant.

Proof. Recalling $L := |x_2 - x_1|$, let $\kappa := L/\Delta t$, and let $s = \lfloor \kappa \rfloor \in \{0, 1, \dots\}$. The piecewise-constant interpolant integrates exactly over the bisected time-step $(t_{n-s}, t_{n+1} - L)$ to give $(s + 1 - \kappa)\Delta t \sigma^{n-s}$. Thus the discretized equations are

$$\sigma_1^{n+1} + \alpha \sum_{\nu \leq n} \sigma_1^\nu + \tilde{\alpha} \sigma_2^{n-s} + \alpha \sum_{\nu < n-s} \sigma_2^\nu = -g_1^{n+1} \quad (58)$$

plus its $1 \leftrightarrow 2$ swapped counterpart, recalling $\alpha := \beta\Delta t/2$, and defining a bisected time-step weight $\tilde{\alpha} := (s + 1 - \kappa)\alpha$. Taking the difference of successive time-steps, any solution to the above satisfies the coupled difference equations

$$\sigma_1^{n+1} + (\alpha - 1)\sigma_1^n + \tilde{\alpha}\sigma_2^{n-s} + (\alpha - \tilde{\alpha})\sigma_2^{n-s-1} = -\Delta g_1^{n+1} \quad (59)$$

plus its $1 \leftrightarrow 2$ swapped counterpart. Its characteristic equation is a 2×2 matrix polynomial, thus we seek stability by considering the solutions $z \in \mathbb{C}$ of

$$\det \begin{bmatrix} z^{s+2} + (\alpha - 1)z^{s+1} & \tilde{\alpha}z + \alpha - \tilde{\alpha} \\ \tilde{\alpha}z + \alpha - \tilde{\alpha} & z^{s+2} + (\alpha - 1)z^{s+1} \end{bmatrix} = 0. \quad (60)$$

This clearly vanishes whenever z is a root of either p_+ or p_- , the scalar polynomials

$$p_\pm(z) := z^{s+2} + (\alpha - 1)z^{s+1} \pm (\tilde{\alpha}z + \alpha - \tilde{\alpha}).$$

Note that $p_-(1) = 0$, giving the factorization

$$p_-(z) = (z - 1)(z^{s+1} + \alpha z^s + \dots + \alpha z + \alpha - \tilde{\alpha})$$

which verifies that 1 is a simple root of p_- , because the remainder polynomial evaluates to $1 + (s+1)\alpha - \tilde{\alpha} > 1 + s\alpha$ when $z = 1$. Also, $p_+(1) = 2\alpha \neq 0$. Thus $z = 1$ is a simple root of the characteristic equation (60).

It remains to prove that all other roots of p_\pm , and hence of (60), lie strictly within $|z| < 1$. The following applies to p_- or p_+ . We apply Rouché’s theorem on the curve Γ_ϵ defined as the boundary of the union of the unit disk $|z| < 1$ and the overlapping disk $|z - 1 + \alpha| < r$, where $r = \alpha + \epsilon$, for $\epsilon > 0$. We choose a comparison polynomial $q(z) := z^{s+2} + (\alpha - 1)z^{s+1}$, whose roots always lie in Γ_ϵ (specifically they are zero with multiplicity $s + 1$, and the simple root $1 - \alpha$). Since q matches the two leading terms

of p_{\pm} , only the degree-1 terms are left, so

$$|p_{\pm}(z) - q(z)| = |\tilde{\alpha}z + \alpha - \tilde{\alpha}| \leq \tilde{\alpha}|z| + \alpha - \tilde{\alpha}, \quad z \in \mathbb{C},$$

since $0 < \tilde{\alpha} \leq \alpha$. Thus $|p_{\pm}(z) - q(z)| \leq \alpha(1 + \epsilon)$ for all $z \in \Gamma_{\epsilon}$, since $|z| \leq 1 + \epsilon$. Yet,

$$|q(z)| = |z^{s+1}| \cdot |z + \alpha - 1|,$$

and the first term is lower-bounded by 1 on Γ_{ϵ} , while the second term is lower-bounded by $r = \alpha + \epsilon$, due to the geometry of the two overlapping disks. Thus a lower bound for $|q|$ on Γ_{ϵ} is $\alpha + \epsilon$, which, by the hypothesis $\alpha < 1$, is strictly larger than the above upper bound on $|p_{\pm} - q|$. Thus Rouché implies that p_{\pm} has $s + 2$ roots in Γ_{ϵ} . The only point on $|z| = 1$ that stays inside Γ_{ϵ} in the limit $\epsilon \rightarrow 0$ is $z = 1$. Thus the $s + 2$ roots must lie in $\{|z| < 1\} \cup \{z = 1\}$. However, we have already shown that $z = 1$ is either a simple root (case p_{-}) or not a root (case p_{+}). Thus all other roots lie in $|z| < 1$.

Recall that p_{-} and p_{+} are the factors of the determinant (60). Then, combining the above, its only root on the unit circle is the simple root $z = 1$, while all $2s + 3$ others lie strictly inside the unit circle. Thus all homogeneous solutions to (59) are constant plus exponentially-decaying components, and thus uniformly bounded. The same thus holds for solutions to (58) for all n beyond which the right-hand sides are zero. \square

A few observations on the above somewhat technical proof are warranted:

1. The difference equation has a larger solution space than the discrete integral equation: it allows a neutrally stable mode (but we do not know whether it is excited in the scattering setting).
2. Attempting to apply Rouché's theorem as usual on a circle $|z| = r$, taking $r \rightarrow 1^{+}$, fails to exclude the possibility of other roots on $|z| = 1$ which may have arbitrarily high multiplicity. This explains the need for the novel contour used.
3. Applying the symmetrization argument used below unfortunately forces a pessimistic stability bound of the form $\Delta t < \mathcal{O}(1/\kappa)$, much worse than achieved above via polynomial roots.

We next prove that 2nd-order time-stepping is stable no matter how large Δt is, for two “nearby” springs in the sense of Section 4.1, meaning $L < \Delta t$ (so the full implicit nature of the scheme is engaged, and the matrix S in (51) is nonzero). For this to hold there is a mild upper bound on L .

Theorem 5.2 (Implicit second-order time-stepping for two springs separated by less than Δt).

Let $L < 2/\beta$, and let $\Delta t > L$. Let $\mathbf{g} := [g_1^1, \dots, g_1^{N_t}, g_2^1, \dots, g_2^{N_t}]$ represent the data vector for N_t time steps. Let $\boldsymbol{\sigma} := [\sigma_1^1, \dots, \sigma_1^{N_t}, \sigma_2^1, \dots, \sigma_2^{N_t}]$ be the vector of densities computed using the discrete Volterra equations arising by applying the linear ($p = 2$) interpolant (55) to (56)–(57), and integrating exactly. Then there is a constant $C > 1$, independent of the data, such that

$$\|\boldsymbol{\sigma}\| \leq C\|\mathbf{g}\|, \tag{61}$$

where $\|\cdot\|$ is the 2-norm on \mathbb{R}^{2N_t} , i.e., the scheme is stable.

Proof. Using $\kappa := L/\Delta t$, $\kappa < 1$, the linear interpolant (55) integrates exactly over the bisected time-step $(t_n, t_{n+1} - L)$ to give $\frac{(1-\kappa)}{2}[(1+\kappa)\sigma^n + (1-\kappa)\sigma^{n+1}]$. The discretized integral equations become

$$\left(1 + \frac{\alpha}{2}\right)\sigma_1^{n+1} + \alpha \sum_{\nu \leq n} \sigma_1^{\nu} + \alpha \sum_{\nu < n} \sigma_2^{\nu} + \xi_1 \sigma_2^n + \xi_2 \sigma_2^{n+1} = -g_1^{n+1}, \tag{62}$$

plus its 1 \leftrightarrow 2 swapped counterpart, defining $\xi_1 := \alpha(2 - \kappa^2)/2$, and $\xi_2 := \alpha(1 - \kappa)^2/2$, again with $\alpha = \beta\Delta t/2$. The scheme in (62) can be expressed as

$$(aI + A)\boldsymbol{\sigma} = -\mathbf{g}, \tag{63}$$

where $a := 1 + \alpha/2$, and A is the $2N_t \times 2N_t$ matrix with lower-triangular blocks given by

$$A = \begin{bmatrix} L_0 & \tilde{L}_0 \\ \tilde{L}_0 & L_0 \end{bmatrix}, \quad L_0 = \begin{bmatrix} 0 & \dots & \dots & 0 \\ \alpha & \ddots & & \vdots \\ \vdots & \ddots & \ddots & \vdots \\ \alpha & \dots & \alpha & 0 \end{bmatrix}, \quad \tilde{L}_0 = \begin{bmatrix} \xi_2 & 0 & \dots & \dots & 0 \\ \xi_1 & \ddots & \ddots & & \vdots \\ \alpha & \ddots & \ddots & \ddots & \vdots \\ \vdots & \ddots & \ddots & \ddots & 0 \\ \alpha & \dots & \alpha & \xi_1 & \xi_2 \end{bmatrix}.$$

We adapt a symmetrization argument from [33, Sec. 4] to show that $\|\boldsymbol{\sigma}\|$ is bounded by the data $\|\mathbf{g}\|$. We multiply Equation (63) by $\boldsymbol{\sigma}^T$ from the left

$$a\|\boldsymbol{\sigma}\|^2 + \boldsymbol{\sigma}^T A \boldsymbol{\sigma} = -\boldsymbol{\sigma}^T \mathbf{g},$$

and note that for $W = A + A^T$, $\boldsymbol{\sigma}^T A \boldsymbol{\sigma} = \frac{1}{2} \boldsymbol{\sigma}^T W \boldsymbol{\sigma}$, so that

$$a\|\boldsymbol{\sigma}\|^2 + \frac{1}{2} \boldsymbol{\sigma}^T W \boldsymbol{\sigma} = -\boldsymbol{\sigma}^T \mathbf{g}. \quad (64)$$

We further partition W into a sum of two matrices V and Q by introducing a positive parameter θ and writing $W = V + Q$. The matrix Q takes the form

$$Q = \alpha \mathbf{1} \mathbf{1}^T - (\alpha + \theta) I, \quad (65)$$

where $\mathbf{1}$ is the $2N_t \times 1$ vector of ones, and I is the $2N_t \times 2N_t$ identity matrix. The matrix V is

$$V = \begin{bmatrix} \theta I & V_1 \\ V_1 & \theta I \end{bmatrix}, \quad (66)$$

where V_1 is tridiagonal with $\omega_2 := 2\xi_2 - \alpha = \alpha\kappa(\kappa - 2)$ on the main diagonal and $\omega_1 := \xi_1 - \alpha = -\kappa^2\alpha/2$ on the sub-diagonals. The spectral norm $\|V_1\|$ at least $|\omega_2 + 2\omega_1| = 2\kappa\alpha$ because this is the eigenvalue for the constant vector, and by Gershgorin's theorem this is also the upper bound, so $\|V_1\| = 2\kappa\alpha$. The block structure of V means that it is positive semi-definite if

$$\theta \geq \|V_1\| = 2\kappa\alpha = L\beta, \quad (67)$$

using the definitions of κ and α . With the partitioning $W = V + Q$, equation (64) yields

$$a\|\boldsymbol{\sigma}\|^2 + \frac{1}{2} \boldsymbol{\sigma}^T (V + \alpha \mathbf{1} \mathbf{1}^T - \alpha I - \theta I) \boldsymbol{\sigma} = -\boldsymbol{\sigma}^T \mathbf{g},$$

but we may drop the nonnegative quantities $\boldsymbol{\sigma}^T \mathbf{1} \mathbf{1}^T \boldsymbol{\sigma} \geq 0$ and $\boldsymbol{\sigma}^T V \boldsymbol{\sigma} \geq 0$, and bound $-\boldsymbol{\sigma}^T \mathbf{g} \leq \|\boldsymbol{\sigma}\| \|\mathbf{g}\|$ by Cauchy–Schwarz, to get

$$\left(1 - \frac{\theta}{2}\right) \|\boldsymbol{\sigma}\| \leq \|\mathbf{g}\|. \quad (68)$$

This bound is only useful if $\theta < 2$; by the hypothesis $L\beta < 2$ this is compatible with (67), and one may pick $\theta = L\beta$. The constant in (61) may thus be chosen as $C = 1/(1 - L\beta/2)$. \square

5.3. A convergence result for two springs

Our final result is convergence of the 2nd-order accurate time-stepping scheme for two springs, in the style of [32, Thm. 7.2] (this theorem cannot be applied directly because of the wave propagation delays in our kernels). Given a time step Δt , let σ_1^n, σ_2^n be the solutions computed using the discrete Volterra equations arising from substituting the linear ($p = 2$) interpolant (55) in (56)–(57), and integrating exactly. Let $\sigma_1(t_n), \sigma_2(t_n)$ be samples of the true solutions of the Volterra equations in (10). Define the error vector at time $t_n = n\Delta t$ to be $\boldsymbol{\varepsilon}^n := [\varepsilon_1^n, \varepsilon_2^n]^T$ where the error at each scatterer is $\varepsilon_j^n := \sigma_j(t_n) - \sigma_j^n$, $j = 1, 2$.

Theorem 5.3. *Let $0 < \Delta t < \min(2/\beta, L)$, and consider the discrete solution error vector defined above, over a fixed solution interval $t \in (0, T)$. Suppose that the densities initially vanish, i.e., $\sigma_{1,2}(0) = 0$.*

Then, using $\|\cdot\|_1$ as the 1-norm on \mathbb{R}^2 ,

$$\|\varepsilon^n\|_1 = \mathcal{O}(\Delta t^2) \quad \text{as } \Delta t \rightarrow 0, \quad \text{uniformly over } 0 \leq n \leq N_t = \lceil T/\Delta t \rceil. \quad (69)$$

Proof. Again set $\kappa = L/\Delta t$, and $s = \lceil \kappa \rceil \geq 1$. Integrating the linear interpolant in (55) over the bisected time-step $(t_{n-s}, t_{n+1} - L)$ gives

$$\frac{\Delta t}{2}(1 - \kappa + s)(1 + \kappa - s)\sigma^{n-s} + \frac{\Delta t}{2}(1 - \kappa + s)^2\sigma^{n-s+1}, \quad (70)$$

so that the discrete equations become

$$\left(1 + \frac{\alpha}{2}\right)\sigma_1^{n+1} + \alpha \sum_{\nu \leq n} \sigma_1^\nu + \alpha \sum_{\nu < n-s} \sigma_2^\nu + \xi_1 \sigma_2^{n-s} + \xi_2 \sigma_2^{n+1-s} = -g_1^{n+1}, \quad (71)$$

plus its 1 \leftrightarrow 2 swapped counterpart, where

$$\begin{aligned} \xi_1 &:= \frac{\alpha}{2} [(1 - \kappa + s)(1 + \kappa - s) + 1], \\ \xi_2 &:= \frac{\alpha}{2} (1 - \kappa + s)^2. \end{aligned} \quad (72)$$

Subtracting (71) from the true integral equation (10) evaluated at t_{n+1} gives

$$\begin{aligned} \varepsilon_1^{n+1} &= -\frac{\beta}{2} \left(\int_0^{t_{n+1}} \sigma_1(\tau) d\tau - \frac{\Delta t}{2} \sigma_1^{n+1} - \Delta t \sum_{\nu \leq n} \sigma_1^\nu \right) \\ &\quad - \frac{\beta}{2} \left(\int_0^{t_{n+1}-L} \sigma_2(\tau) d\tau - \Delta t \sum_{\nu < n-s} \sigma_2^\nu - \tilde{\xi}_1 \sigma_2^{n-s} - \tilde{\xi}_2 \sigma_2^{n-s+1} \right), \end{aligned} \quad (73)$$

and its 1 \leftrightarrow 2 swapped counterpart, where $\tilde{\xi}_\ell := (2/\beta)\xi_\ell$, $\ell = 1, 2$. Define the local consistency errors

$$\begin{aligned} \Delta_1^{n+1} &= \int_0^{t_{n+1}} \sigma_1(\tau) d\tau - \frac{\Delta t}{2} \sigma_1(t_{n+1}) - \Delta t \sum_{\nu \leq n} \sigma_1(t_\nu), \\ \tilde{\Delta}_2^{n+1} &= \int_0^{t_{n+1}-L} \sigma_2(\tau) d\tau - \Delta t \sum_{\nu < n-s} \sigma_2(t_\nu) - \tilde{\xi}_1 \sigma_2(t_{n-s}) - \tilde{\xi}_2 \sigma_2(t_{n-s+1}), \end{aligned} \quad (74)$$

along with the 1 \leftrightarrow 2 swapped counterparts. By design of the 2nd-order accurate quadrature scheme, noting that no endpoint correction is needed at $t = 0$ due to the densities vanishing there, we have

$$\max_{0 \leq n \leq N_t} |\Delta_1^n| \leq c\Delta t^2, \quad \max_{0 \leq n \leq N_t} |\tilde{\Delta}_2^n| \leq \tilde{c}\Delta t^2, \quad (75)$$

where c and \tilde{c} are constants. The error equation in (73) becomes

$$\begin{aligned} \varepsilon_1^{n+1} &= -\frac{\beta}{2} \left(\Delta_1^{n+1} + \frac{\Delta t}{2} \varepsilon_1^{n+1} + \Delta t \sum_{\nu \leq n} \varepsilon_1^\nu \right) \\ &\quad - \frac{\beta}{2} \left(\tilde{\Delta}_2^{n+1} + \Delta t \sum_{\nu < n-s} \varepsilon_2^\nu + \tilde{\xi}_1 \varepsilon_2^{n-s} + \tilde{\xi}_2 \varepsilon_2^{n-s+1} \right). \end{aligned} \quad (76)$$

Noting that $|\tilde{\xi}_1|, |\tilde{\xi}_2| \leq \Delta t$, we write

$$\left(1 - \frac{\beta\Delta t}{4}\right) |\varepsilon_1^{n+1}| \leq \frac{\beta}{2} \left(|\Delta_1^{n+1}| + |\tilde{\Delta}_2^{n+1}| \right) + \frac{\Delta t\beta}{2} \sum_{\nu \leq n} (|\varepsilon_1^\nu| + |\varepsilon_2^\nu|). \quad (77)$$

We then have

$$\left(1 - \frac{\beta\Delta t}{4}\right) \|\boldsymbol{\varepsilon}^{n+1}\|_1 \leq \frac{\beta}{2} \left(|\Delta_1^{n+1}| + |\Delta_2^{n+1}| + |\tilde{\Delta}_1^{n+1}| + |\tilde{\Delta}_2^{n+1}| \right) + \Delta t \beta \sum_{\nu \leq n} \|\boldsymbol{\varepsilon}^\nu\|_1. \quad (78)$$

By consistency, there exists a constant C such that

$$|\Delta_1^{n+1}| + |\Delta_2^{n+1}| + |\tilde{\Delta}_1^{n+1}| + |\tilde{\Delta}_2^{n+1}| \leq C\Delta t^2, \quad \forall n = 0, \dots, N_t - 1.$$

Provided that $\beta\Delta t < 4$, we may write the inequality in (78) as

$$\|\boldsymbol{\varepsilon}^{n+1}\|_1 \leq \frac{\beta}{2\left(1 - \frac{\beta\Delta t}{4}\right)} C\Delta t^2 + \frac{\Delta t \beta}{\left(1 - \frac{\beta\Delta t}{4}\right)} \sum_{\nu \leq n} \|\boldsymbol{\varepsilon}^\nu\|_1. \quad (79)$$

Applying the discrete Gronwall inequality [32, Thm. 7.1], we have

$$\|\boldsymbol{\varepsilon}^n\|_1 \leq \frac{\beta}{2\left(1 - \frac{\beta\Delta t}{4}\right)} C\Delta t^2 \exp\left(\frac{\beta\Delta t n}{1 - \frac{\beta\Delta t}{4}}\right). \quad (80)$$

Specifically, for $\beta\Delta t < 2$, since $n\Delta t < T$, we arrive at the following estimate

$$\|\boldsymbol{\varepsilon}^n\|_1 \leq \beta C \Delta t^2 e^{2\beta T}. \quad (81)$$

This proves the claim. \square

6. Numerical tests and examples

We demonstrate the high-order convergence and computational performance of the WFP method using numerical examples. In section 6.1, we use the method of manufactured solutions to generate convergence results, while section 6.2 investigates the computational performance of the scheme for free-space spring scattering problems. We investigate physical properties of scattering from randomly placed springs in Section 6.3, demonstrating wave localization. We finish with demonstrations of narrow-band (high-Q) filtering by systems of equi-spaced springs in Section 6.4.

In all experiments we choose window tolerance parameter $\epsilon = 10^{-12}$, and Nyquist fraction $\gamma = 0.5$, as described in section 2. For nonuniform FFTs we use the FINUFFT library [34, 35], which exploits shared-memory parallelism. Our implementation is in MATLAB (using version R2023b), and the local evaluation is done by precomputing a sparse matrix which acts on the stack of the recent m_{\max} density vectors. Tests are run on an Apple M2 Max laptop (released 2023) with 64 GB RAM, apart from the scaling test of section 6.2 which is run on a Ice Lake node with two 32-core Xeon Platinum 8362 2.8 GHz CPUs (released 2021) and 1024 GB RAM.

6.1. Convergence test

To assess the convergence of the WFP method described in sections 2–4 we use the method of manufactured solutions: we generate a free-space scattered potential u_{ex} from analytic densities, read off its data $g_j(t)$, apply the WFP method to solve numerically the free-space Volterra integral equations (10) with this data, then from the resulting solution densities evaluate a new scattered potential u . We report the error $u - u_{\text{ex}}$. The point is to compare to an analytic solution, noting that no analytic solution is known for actual scattering problems.

We place the scatterers uniformly at random at locations $x_j \in [-1, 1]$, enforcing a minimum separation of 10^{-4} between any two scatterers. As densities we choose Gaussian pulses

$$\sigma_j(t) = e^{-\mu_j(t-t_{0,j})^2}, \quad j = 1, \dots, M,$$

with random values assigned to the inverse variances $\mu_j \in [40, 50]$ and peak times $t_{0,j} \in [1, 3]$. These densities generate $u_{\text{ex}} = \mathcal{S}[\Gamma, \vec{\sigma}]$ according to the representation (7). We assign random spring strengths

$\beta_j \in [0.1, 3]$, for $j = 1, \dots, M$. The data $g_j(t), j = 1, \dots, M$, is then extracted as

$$g_j(t) = -\sigma_j(t) - \beta u_{\text{ex}}(x_j, t), \quad (82)$$

recalling (5) and the jump relation (9).

In Figure 4 we use this to test the WFP method convergence with respect to Δt , at $p = 2, 4, 6, 8$ interpolation nodes as defined in Section 4.1. The maximum error between scattered field u and u_{ex} is measured over a uniform space-time grid of size 10×10 , covering $0 < t < T = 6\pi$. We observe errors $\mathcal{O}((\Delta t)^{p+1})$, that is, one order higher than the order- p polynomial interpolation in Section 4.1. The additional Δt factor appears in the local quadrature error since we are making an $\mathcal{O}((\Delta t)^p)$ error on an interval of size $\mathcal{O}(\Delta t)$. In our Volterra integral equation, this local quadrature error dominates the total error since the history part is computed with spectral accuracy. As expected, this algebraic convergence stops at the window tolerance $\mathcal{O}(\epsilon)$, and we note that the scaling with the number of scatterers is well explained by $M\epsilon$.

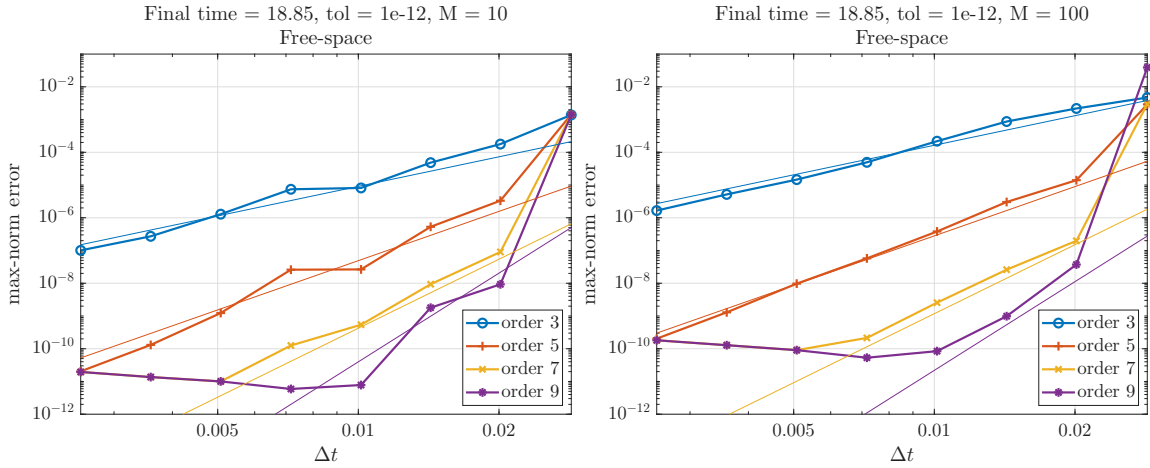


Figure 4: Convergence to a manufactured solution, for the WFP method at interpolation orders $p = 2, 4, 6, 8$. The observed orders $p + 1$ are shown by the thin reference lines. Left plot shows $M = 10$ springs; right plot shows $M = 100$ springs. Convergence bottoms out near the window tolerance $\epsilon = 10^{-12}$. See section 6.1 for details.

6.2. Scaling of CPU time with problem size

Here we measure the computational performance of WFP for large numbers of scatterers M . We choose sources randomly located in $[-2, 2]$ with minimum separation of 10^{-6} between any two sources, and random spring constants $\beta_j \in [0.1, 3]$. In this and the following sections we solve the free-space scattering problem with Gaussian incident pulse

$$f(t) = e^{-\mu(t-t_0)^2}, \quad (83)$$

giving the incident wave (1). In this section we set $\mu = 30$ and $t_0 = -3$. For each M , we select Δt such that $M_{\text{typ}} \approx 100$ (see section 4.3). We set $p = 6$ interpolation nodes (7th-order scheme). This typically gives an accuracy of 10 digits at smaller M , dropping to 6 digits at $M = 10^6$. We report the CPU time required per time-step, and in this section run experiments on the Xeon node described above. This does not include (history and local) evaluation at target points, which becomes negligible at large M . We do not report precomputation time, since it is less than 100 times the cost of one time-step, and in all of our experiments this is negligible compared to the total cost.

Figure 5 shows the results: they are consistent with a cost asymptotically linear in M , approaching a throughput of about 150000 scatterer-time-steps per second. The time-step is dominated by a sparse matrix-vector multiplication and a pair of NUFFT. Note that since K for the Fourier series grows like $1/\Delta t$, which grows like M in order to keep M_{typ} fixed, the NUFFT should cause the complexity to be dominated by $\mathcal{O}(M \log M)$ work per time-step. However, it appears that even at the largest $M = 10^6$ tested, this dominance is not yet visible. The storage is relatively mild: the example with a million scatterers needs only around 2 GB RAM.

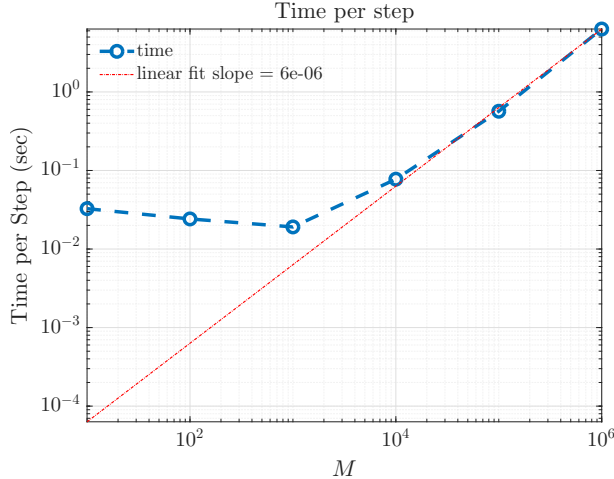


Figure 5: Computational cost per time-step, on a Xeon compute node, for the 7th-order accurate implementation of the WFP scheme as a function of M , the number of spring scatterers. See section 6.2 for details.

6.3. Scattering in 1D disordered media

It is a famous result that a spatially-varying random potential can induce localization of quantum waves [36]. Similar effects occur in acoustic and photonic (wave equation) systems in random media. The 1D case, where localization is strongest, is of interest in physics [3, 5, 6]. In 1D all frequencies are expected to localize, meaning the absence of propagation in an unbounded random medium, and trapping at sites. The amplitude decays exponentially away from such sites, on average, defining a “localization length”, which may depend on frequency [37].

In this section, we study scattering from large numbers of springs at random locations to explore wave localization, and to demonstrate our solver’s wide-band capability in challenging problems. We use the WFP method to solve numerically the free-space scattering problem from the introduction, with the Gaussian incident pulse (1) defined in (83). We take $x_j \in [-2, 2]$ to be randomly spaced, such that the minimum distance between any two scatterers is 10^{-4} . For additional disorder we choose the spring constants β_j randomly.

Figure 6 plots the computed total field $u_{\text{tot}} = u + u_{\text{inc}}$ with space horizontally and time vertically (a “space-time” diagram), computed on a 400×400 regular grid, for $M = 150$ scatterers. Three different random ranges of spring strength are tested (see caption). The pulse parameters in (83) were $\mu = 30$ and $t_0 = -3$. We fix the time step Δt such that $M_{\text{typ}} \approx 10$, and run the simulation up to a final time of $T = 10\pi$. The compute time (see caption) is very modest, less than a minute. A self-convergence study is performed (comparing to a simulation using $\Delta t/2$), giving the estimated uniform errors stated at the top of each plot: the solutions have around 10 digits accuracy.

We observe that the high frequency part of the incident pulse passes through with little delay in the left and middle cases in Figure 6, whereas lower frequency waves are reflected, or trapped for long times inside the spring region. Clear resonant trapping at sites is visible in the right-most case. Here, almost all of the incident wave is reflected at the first bounce. This can be explained as follows, without invoking localization.

Remark 6.1 (Homogenization theory for frequency filtering). *We apply a simple homogenization argument to the wave equation (2) with a dense random set of springs (5), whose mean separation is Δx and mean strength $\bar{\beta}$. Replacing the springs with a distributed spring with the same mean restoring force per unit length gives the Klein-Gordon equation*

$$\partial_t^2 u - \partial_x^2 u + \omega_0^2 u = 0, \quad \text{where } \omega_0^2 = \bar{\beta}/\Delta x, \quad (84)$$

as an effective PDE for the region $[-2, 2]$. Here ω_0 is the cut-off frequency below which waves cannot propagate (the dispersion relation is $\omega = \sqrt{\omega_0^2 + \kappa^2}$). Applying this to the three strength distributions in Figure 6 gives $\omega_0 \approx 7.6$ for the first case, rising to $\omega_0 \approx 13.8$ for the third case. The incident frequency content is the Gaussian $\hat{f}(\omega) \propto e^{-\omega^2/4\mu}$, which has standard deviation $\sqrt{2\mu} \approx 7.7$. Thus in the first case a significant portion of the incident frequencies lie above ω_0 , explaining the propagation of high frequencies

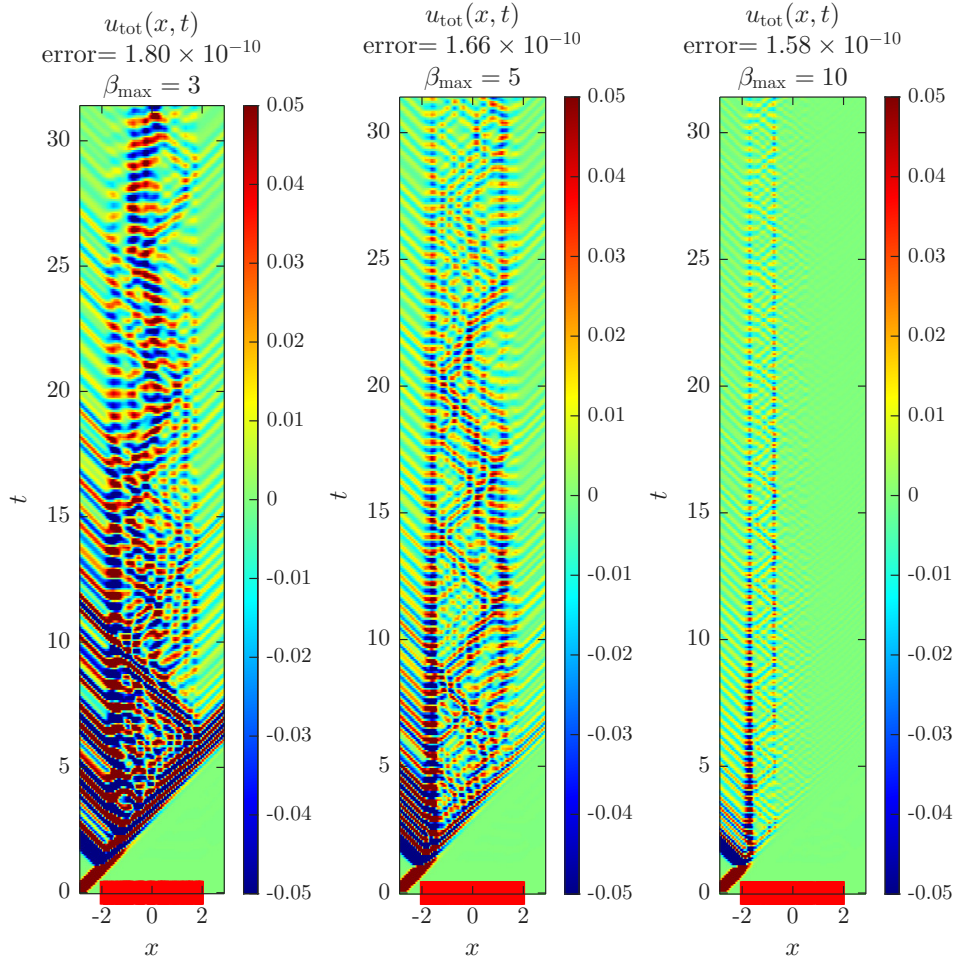


Figure 6: 9th-order accurate ($p = 8$) computed total field when scattering from a region containing $M = 150$ randomly located springs (appearing as a dense red block), with random strengths $\beta_j \in [0.1, 3]$ (left), $\beta_j \in [0.1, 5]$ (middle), or $\beta_j \in [0.1, 10]$ (right). The time step is $\Delta t = 3.703 \times 10^{-3}$. This takes about 40 seconds of CPU time to compute (of which 0.6 is precomputation), using $N_t = 8484$ time-steps.

right through the spring region. In the last case ω_0 is nearly at two standard deviations, explaining why very little energy propagates through the medium.

Figure 7 shows challenging examples with large numbers of random springs: $M = 10^3$ (left) and $M = 10^4$ (right). As M grows, Δt must decrease in order that the number of local neighbors M_{typ} remain $\mathcal{O}(1)$ to keep the method linear-scaling (in other words, a longer Δt would not be cheaper, due to the local cost), but also for stability reasons. However, this means that the scheme can accurately handle a growing incident wave bandlimit of $\mathcal{O}(M)$. We thus choose the incident pulse to have a width $\mathcal{O}(1/M) = \mathcal{O}(\Delta x)$, by setting $\mu = M^2$. Regardless of M , such a pulse has a standard deviation (width) $\sqrt{8}$ times the mean inter-spring spacing $\Delta x = 4/M$. As before, $t_0 = -3$. The spring constants β_j are chosen randomly from the interval $[0.1, 3]$, and Δt is such that the typical number of neighbors for each source is $M_{\text{typ}} = 50$ for $M = 10^3$, and $M_{\text{typ}} = 500$ for $M = 10^4$.

We observe complex multiple reflections, dispersion (of a strong transmitted wave), and trapping; a full study is beyond this paper. Since $\mathcal{O}(M)$ time-steps are needed to simulate a couple of wave passage times, the total simulation cost grows like $\mathcal{O}(M^2 \log M)$. This is apparent since growing M by a factor of 10 turns a 24-minute run into a 28-hour run. By comparing against runs at $\Delta t/2$, the estimated errors are over nine digits for $M = 10^3$, and over eight digits for $M = 10^4$.

6.4. Scattering and filtering by periodic arrays of springs

Regular 1D arrays of identical scatterers are commonly used for filtering of waves (e.g., the distributed Bragg filter). Here we apply the WFP scheme to solve scattering problems of this form. We observe the

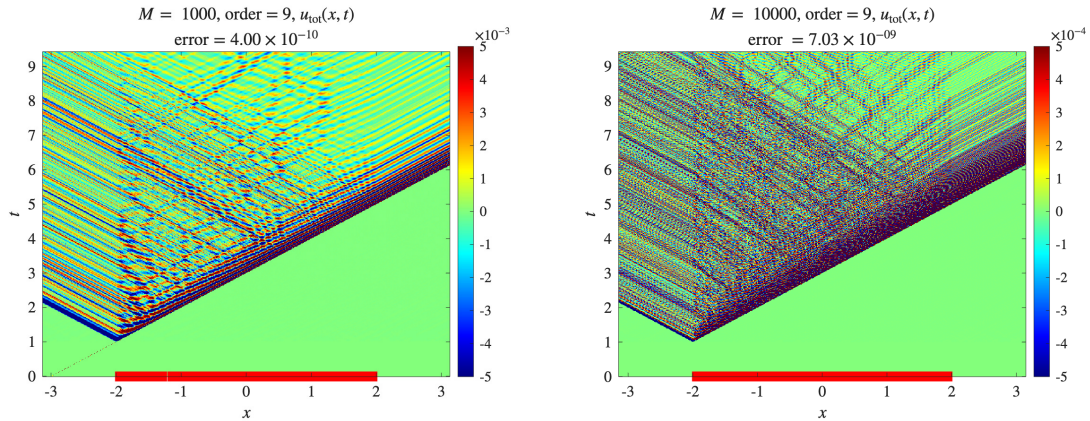


Figure 7: Ninth-order accurate computed total field for a narrow incident wave with $\mu = M^2$ and $M = 10^3$ (left) or $M = 10^4$ (right) random spring scatterers. The incident wave is almost too narrow to see in either plot. For $M = 10^3$, $\Delta t = 1.308 \times 10^{-4}$, and the runtime is 24 minutes (1.2 sec for precomputation), and 0.02 sec per time-step for $N_t = 72044$ total time steps. For $M = 10^4$, $\Delta t = 1.308 \times 10^{-5}$, and the runtime is 29.5 hours (9 sec precomputation), at 0.15 sec per time-step for $N_t = 720440$ time steps.

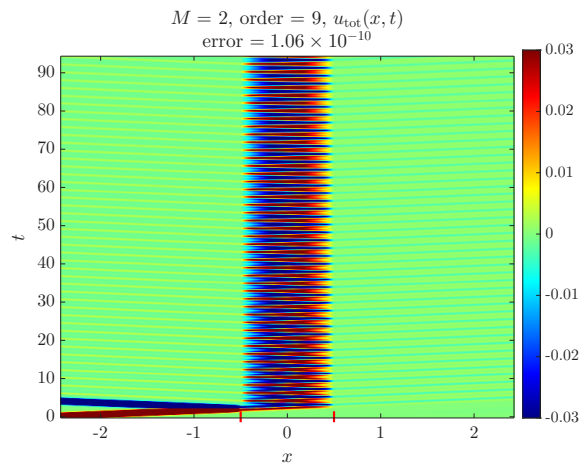


Figure 8: Scattering from two springs (indicated by red tick marks on the x -axis) a unit distance apart, with spring constants $\beta = 100$. Note that most of the incident energy is reflected; what passes through is very narrow in frequency. This simple simulation takes 16 seconds, with $N_t = 9426$ time steps of $\Delta t = 0.01$. See Section 6.4.

transmission filtering, meaning the temporal Fourier transform of the total wave $u(x, \cdot)$ at a target point x downstream of the device, as compared to the Fourier transform of the incident pulse f .

The filtering effect depends on the number of sources and the choice of spring constants. For example, given an incident wave of the form (83) with $\mu = 5$ and $t_0 = -3$, Figure 8 presents the order 9-accurate total field with two springs located at $x_1 = -0.5$ and $x_2 = 0.5$, and large strengths $\beta_1 = \beta_2 = 100$. This arrangement of two highly-reflective (near-Dirichlet) scatterers is common in optics, and is known as a Fabry–Perot interferometer. Waves get trapped between the two springs; only waves with frequencies ω close to multiples of π/L are transmitted, $L = x_2 - x_1 = 1$ being the cavity length. Figure 9 compares the Fourier transforms (approximated via the windowed FFT) of the incident and transmitted signals for this device.

Figure 10 illustrates experiments with larger period spring arrays with an incident pulse of the form (83) where $\mu = 5$ and $t_0 = -4$. The estimated accuracies (via self-convergence using $\Delta t/2$) are again around 9–10 digits and the run times quite short (see caption and uniform error figures above the plots). Interesting cavity-coupling behaviors are seen whose understanding we leave for future work.

We believe that the examples in this section highlight the ease of accurate wide-band 1D wave simulations with large numbers of point scatterers.

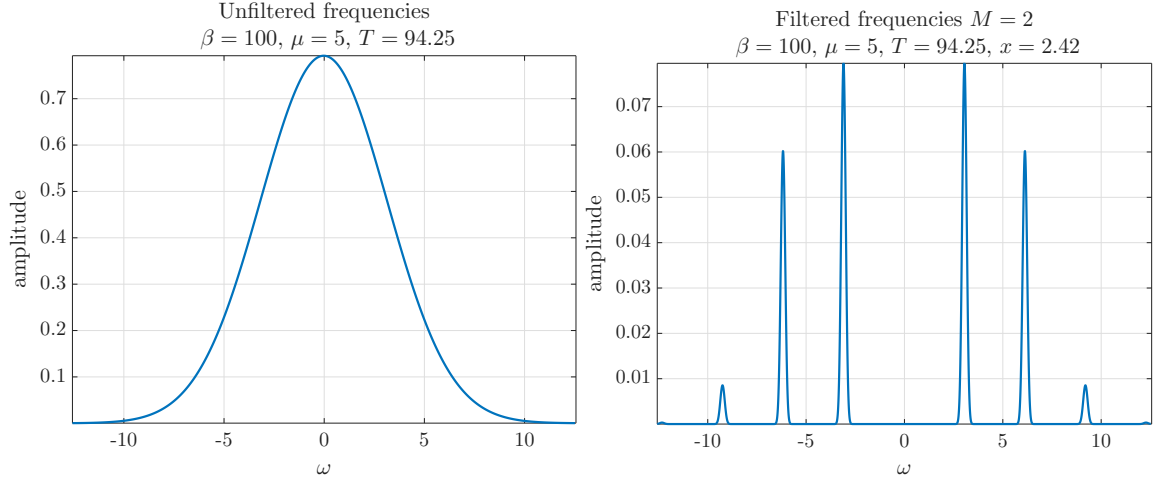


Figure 9: Spectra of the incident wave (left) and the windowed total solution (right) after passing through the $M = 2$ Fabry-Perot filter as in Figure 8.

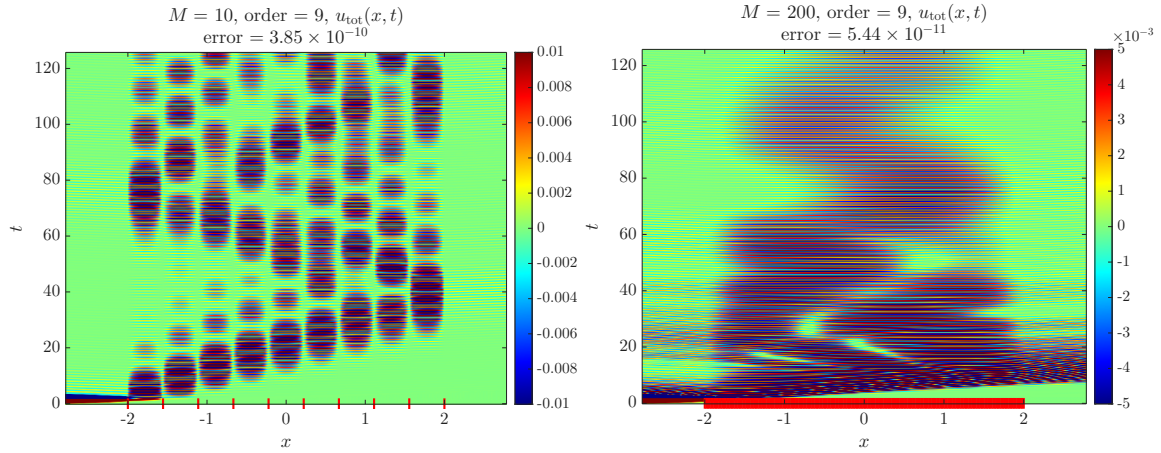


Figure 10: Scattering from M uniformly spaced springs (red tick marks on the x -axis) with equal strengths β . The total field is shown, the scheme is 9th order ($p = 8$), and the estimated accuracies are as shown above the plots. Left: $M = 10$ with $\beta = 100$; runtime is 91 seconds. Right: $M = 200$ with $\beta = 1$; runtime is 114 seconds. In both cases 25134 time-steps were used.

7. Conclusions and discussion

We have presented a fast spectrally-accurate history compression scheme (WFP) for hyperbolic layer potentials for the wave equation. It reduces the quadratic costs in the number of sources, and in the number of time steps, both to linear, with a new cost quasilinear in the number of wavelengths across the domain. We applied it to the arbitrary-order accurate solution of problems where 1D waves impinge on a large number of point-like scatterers that physically model springs attached to a string, with applications in disordered acoustics and optical systems. We showed time-dependent solutions for up to 10000 springs with many accurate digits, and demonstrated the expected cost scaling per time step for up to a million springs. The scheme would easily incorporate nonlinear scatterers, unlike solvers that Fourier transform in time (which are intrinsically linear). The generalizations to 2D and 3D, where point scatterers are replaced by surface quadrature nodes, are already in progress—although for free-space boundary conditions they involve new techniques—and will be reported on soon.

The main analytic results are: 1) a proof that for bandlimited densities WFP is spectrally convergent with respect to Fourier truncation (Theorem 1), and 2) various stability and convergence results for the 1st- and 2nd-order cases for two springs (Section 5). One future goal is replacing conditions on the densities in Theorem 1 with conditions on the incident wave in the BVP; due to causality, this will demand more nuanced spaces than strict bandlimited functions. It would also be interesting to try to generalize our eigenvalue-based stability proofs to 2nd-order for well-separated springs, orders $p > 2$, and

$M > 2$ springs.

Appendix A. Proof of Theorem 1 on Fourier truncation

We use Fourier transforms as defined in (32). The Kaiser–Bessel window derivative ϕ' in (30) has, applying (29), the Fourier transform

$$\hat{\phi}'(\omega) = \frac{be^{-i\delta\omega/2}}{\sinh b} \operatorname{sinc} \sqrt{\left(\frac{\delta\omega}{2}\right)^2 - b^2}, \quad \omega \in \mathbb{R} \quad (\text{A.1})$$

We now fix $k \in \mathbb{Z}$, with $|k| > K$. The Fourier transform of the k th influence kernel is related to that of the window derivative by

$$\hat{\Psi}_k(\omega) = \left(1 - \frac{\omega}{2k}\right) \hat{\phi}'(\omega + k) + \left(1 + \frac{\omega}{2k}\right) \hat{\phi}'(\omega - k), \quad k \in \mathbb{Z} \setminus \{0\}, \omega \in \mathbb{R}, \quad (\text{A.2})$$

a formula easily derived from (37) and using the Fourier transform of a derivative. Note that the multiplication by sinusoids in (37) shifted the center frequency of the window from zero to $\pm k$. In particular, for the Kaiser–Bessel window inserting (A.1) gives

$$\hat{\Psi}_k(\omega) = \frac{be^{-i\delta\omega/2}}{\sinh b} \left[\left(1 - \frac{\omega}{2k}\right) \operatorname{sinc} \sqrt{(\delta(\omega + k)/2)^2 - b^2} + \left(1 + \frac{\omega}{2k}\right) \operatorname{sinc} \sqrt{(\delta(\omega - k)/2)^2 - b^2} \right]. \quad (\text{A.3})$$

Now, by the hypothesis $|k| > K \geq K_0 + 2b/\delta$, the signal frequencies $\omega \in [-K_0, K_0]$ lie outside of both shifted window cutoff bands $[k - 2b/\delta, k + 2b/\delta]$ and $[-k - 2b/\delta, -k + 2b/\delta]$; that is, the arguments of the sinc functions are real-valued, so we may apply $|\operatorname{sinc} x| \leq 1/x$. Thus, doubling the larger of the two $\pm k$ terms, and noting $1 + \omega/2k < 3/2$,

$$\max_{-K_0 \leq \omega \leq K_0} |\hat{\Psi}_k(\omega)| \leq \frac{2b}{\sinh b} \frac{3/2}{\sqrt{(\delta(|k| - K_0)/2)^2 - b^2}}. \quad (\text{A.4})$$

Now consider the driving function F_k given by (36). The convolution theorem gives $\hat{F}_k(\omega) = \hat{\Psi}_k(\omega) \hat{S}_k(\omega)$, and, since S_k has bandlimit K_0 ,

$$\|\hat{F}_k\|_{L^2(\mathbb{R})} \leq \max_{-K_0 \leq \omega \leq K_0} |\hat{\Psi}_k(\omega)| \cdot \|\hat{S}_k\|_{L^2(\mathbb{R})} \leq \frac{b}{\sinh b} \frac{3\sqrt{2\pi}MC}{\sqrt{(\delta(|k| - K_0)/2)^2 - b^2}} \quad (\text{A.5})$$

where in the 2nd step we applied the following bound using Parseval's theorem, the definition (18), Cauchy–Schwarz, and the hypothesis that the densities have bounded norm,

$$\frac{1}{2\pi} \|\hat{S}_k\|_{L^2(\mathbb{R})}^2 = \|S_k\|_{L^2(\mathbb{R})}^2 \leq \int_{\mathbb{R}} \left| \sum_{j=1}^M \sigma_j(t) e^{-ikx_j} \right|^2 dt \leq M \int_{\mathbb{R}} \sum_{j=1}^M |\sigma_j(t)|^2 dt = M \sum_{j=1}^M \|\sigma_j\|_{L^2(\mathbb{R})}^2 \leq M^2 C^2.$$

Observe that the Duhamel principle for the ODE system (38) with initial conditions $\alpha_k(0) = \alpha'_k(0) = 0$ gives a new formula for α_k as a convolution of F_k with the propagator,

$$\alpha_k(t) = \int_0^t \frac{\sin k(t - \tau)}{k} F_k(\tau) d\tau \quad (\text{A.6})$$

(contrast the formulae (26) and (36)). Applying Young's convolution inequality [38, §4.2] over $0 < t < T$,

$$\|\alpha_k\|_{L^2(0,T)} \leq \left\| \frac{\sin k \cdot}{k} \right\|_{L^1(0,T)} \|F_k\|_{L^2(0,T)} \leq \frac{b}{\sinh b} \frac{3MCT}{k\sqrt{(\delta(|k| - K_0)/2)^2 - b^2}} \quad (\text{A.7})$$

where we used $\|\sin k \cdot\|_{L^1(0,T)} \leq T$, Parseval's theorem, and (A.5).

We finally now sum over k : applying the triangle inequality in $L^2(0, T)$ to (33), using (A.7) gives

$$\|E_K\|_{L^2(0,T)} \leq \sum_{|k|>K} \|\alpha_k\|_{L^2(0,T)} \leq 6MCT \frac{b}{\sinh b} \cdot \frac{2}{\delta} \sum_{k=K+1}^{\infty} \frac{1}{k\sqrt{(k-K_0)^2 - (2b/\delta)^2}}. \quad (\text{A.8})$$

Shifting the index to $y = k - K_0 - 2b/\delta$ turns this sum into

$$\sum_{y=K-K_0-2b/\delta+1}^{\infty} \frac{1}{(y+K_0+2b/\delta)\sqrt{(y+2b/\delta)^2 - (2b/\delta)^2}} \leq \sum_{y=K-K_0-2b/\delta+1}^{\infty} \frac{1}{y \cdot y} \leq \frac{\pi^2}{6},$$

noting that the sum is over an arithmetic sequence of unit spacing starting no smaller than 1, using the hypothesis (34) on K . Substituting the sum bound into (A.8) gives (35), and the proof is complete.

A couple of notes on the proof are worth mentioning:

- It is tempting to replace (A.6) by the original definition (26), but there would be an obstacle since the windowed propagator $\phi(\cdot) \sin k \cdot$ is not in $L^2(\mathbb{R})$.
- The algebraic prefactors can undoubtedly be improved, for instance by splitting the k sum (A.8) into two parts handled separately. This would not, however, improve the asymptotic exponential rate e^{-b} .

References

- [1] W. C. Chew, J.-M. Jin, E. Michielssen, J. Song, *Fast and Efficient Algorithms in Computational Electromagnetics*, Artech House, Boston, MA, USA, 2001.
- [2] R. Guenther, J. Lee, *Partial Differential Equations of Mathematical Physics and Integral Equations*, Dover Books on Mathematics, Dover Publications, 2012.
- [3] C. H. Hodges, J. Woodhouse, Vibration isolation from irregularity in a nearly periodic structure: theory and measurements, *J. Acoust. Soc. Am.* 74 (1983) 894–905.
- [4] P. A. Martin, *Time-domain scattering*, Cambridge University Press, 2021.
- [5] C. A. Condat, T. R. Kirkpatrick, Localization and resonant transmission of third-sound waves on a random substrate, *Phys. Rev. B* 33 (5) (1986) 3102–3114.
- [6] O. Richoux, E. Morand, L. Simon, Analytic study of the propagation of acoustic waves in a 1D weakly disordered lattice, *Ann. Phys.* 324 (2009) 1983–1995.
- [7] O. Richoux, C. Depollier, J. Hardy, Propagation of mechanical waves in a one-dimensional nonlinear disordered lattice, *Phys. Rev. E* 73 (2006) 026611.
- [8] S. Albeverio, F. Gesztesy, R. Hoegh-Krohn, H. Holden, *Solvable models in quantum mechanics*, Springer Science & Business Media, 2012.
- [9] J. Holmer, J. Marzuola, M. Zworski, Fast soliton scattering by delta impurities, *Commun. Math. Phys.* 274 (2007) 187–216.
- [10] A. H. Barnett, L. Greengard, T. Hagstrom, High-order discretization of a stable time-domain integral equation for 3D acoustic scattering, *J. Comput. Phys.* 402 (2020) 109047.
URL <https://www.sciencedirect.com/science/article/pii/S0021999119307521>
- [11] L. Greengard, J. Strain, A fast algorithm for the evaluation of heat potentials, *Commun. Pure Appl. Math.* 43 (1990) 949–963.
- [12] J. Kaye, A. H. Barnett, L. Greengard, A high-order integral equation-based solver for the time-dependent Schrödinger equation, *Commun. Pure Appl. Math.* 75 (8) (2022) 1657–1712.
URL <https://onlinelibrary.wiley.com/doi/abs/10.1002/cpa.21959>
- [13] A. Soffer, C. Stucchio, Open boundaries for the nonlinear Schrödinger equation, *J. Comput. Phys.* 225 (2) (2007) 1218–1232.
URL <https://www.sciencedirect.com/science/article/pii/S0021999107000368>
- [14] C. Stucchio, A. Soffer, Multiscale resolution of shortwave-longwave interaction, *Commun. Pure Appl. Math.* 62 (1) (2009) 82–124.
- [15] A. Soffer, C. Stucchio, M.-B. Tran, *Time Dependent Phase Space Filters: A Stable Absorbing Boundary Condition*, Springer Briefs on PDEs and Data Science, Springer Nature, 2023.
- [16] E. Hairer, C. Lubich, M. Schlichte, Fast numerical solution of nonlinear volterra convolution equations, *SIAM Journal on Scientific and Statistical Computing* 6 (3) (1985) 532–541.
URL <https://doi.org/10.1137/0906037>
- [17] J. Tausch, A fast method for solving the heat equation by layer potentials, *J. Comput. Phys.* 224 (2) (2007) 956–969.
URL <https://doi.org/10.1016/j.jcp.2006.11.001>
- [18] B. Shanker, A. A. Ergin, M. Lu, E. Michielssen, Fast analysis of transient electromagnetic scattering phenomena using the multilevel plane wave time domain algorithm, *IEEE Transactions on Antennas and Propagation* 51 (3) (2003) 628–641.
- [19] J. Kaiser, Digital filters, in: J. Kaiser, F. Kuo (Eds.), *System analysis by digital computer*, Wiley, 1966, Ch. 7, pp. 218–285.
- [20] F. Oberhettinger, *Tables of Fourier transforms and Fourier transforms of distributions*, Springer-Verlag, 1990.

- [21] A. H. Barnett, How exponentially ill-conditioned are contiguous submatrices of the Fourier matrix?, *SIAM Rev.* 64 (1).
- [22] D. Slepian, H. O. Pollak, Prolate spheroidal wave functions, Fourier analysis and uncertainty, I, *Bell Syst. Tech. J.* 40 (1961) 43–64.
- [23] A. H. Barnett, Aliasing error of the $\exp(\beta\sqrt{1-z^2})$ kernel in the nonuniform fast Fourier transform, *Appl. Comput. Harmon. Anal.* 51 (2021) 1–16.
- [24] L. N. Trefethen, J. A. C. Weideman, The exponentially convergent trapezoidal rule, *SIAM Rev.* 56 (3) (2014) 385–458.
- [25] G. Dahlquist, A. Björck, *Numerical Methods in Scientific Computing, Volume I, Other Titles in Applied Mathematics*, Society for Industrial and Applied Mathematics, 3600 Market Street, Floor 6, Philadelphia, PA 19104, 2008.
- [26] A. Dutt, V. Rokhlin, Fast Fourier transforms for nonequispaced data, *SIAM J. Sci. Comput.* 14 (1993) 1368–1393.
- [27] A. Dutt, V. Rokhlin, Fast Fourier transforms for nonequispaced data. II, *Appl. Comput. Harmon. Anal.* 2 (1995) 85–100.
- [28] L. Greengard, J. Lee, Accelerating the nonuniform fast Fourier transform, *SIAM Rev.* 46 (2004) 443–454.
- [29] N. G. Al Hassanieh, A. H. Barnett, MATLAB implementation of windowed Fourier projection (2025).
URL <https://github.com/nalhassanieh/windowedFourierProjection.git>
- [30] T. Hagstrom, Radiation boundary conditions for the numerical simulation of waves, in: *Acta numerica*, 1999, Vol. 8 of *Acta Numer.*, Cambridge Univ. Press, Cambridge, 1999, pp. 47–106.
- [31] V. S. Ryaben’kii, S. V. Tsynkov, V. I. Turchaninov, Global discrete artificial boundary conditions for time-dependent wave propagation, *J. Comput. Phys.* 174 (2001) 712–758.
- [32] P. Linz, *Analytical and numerical methods for Volterra equations*, Studies in Applied and Numerical Mathematics, number 7, SIAM, Philadelphia, 1985.
- [33] A. H. Barnett, C. L. Epstein, L. F. Greengard, S. Jiang, J. Wang, Explicit unconditionally stable methods for the heat equation via potential theory, *Pure Appl. Anal.* 1 (4) (2019) 709–742.
- [34] A. H. Barnett, J. Magland, L. af Klinteberg, A parallel non-uniform fast Fourier transform library based on an “exponential of semicircle” kernel, *SIAM J. Sci. Comput.* 41 (2019) C479–C504.
- [35] A. H. Barnett, *et al.*, Flatiron Institute Nonuniform Fast Fourier Transform (2018–2025).
URL <https://github.com/flatironinstitute/finufft>
- [36] P. W. Anderson, Absence of diffusion in certain random lattices, *Phys. Rev.* 109 (8) (1958) 1492–1505.
- [37] V. Freilikher, S. Gredeskul, III. Localization of waves in media with one-dimensional disorder, Vol. 30 of *Prog. Opt.*, Elsevier, 1992, pp. 137–203.
- [38] E. H. Lieb, M. Loss, *Analysis*, 2nd Edition, Graduate Studies in Mathematics, Volume 14, AMS, Providence, RI, 2001.